Ocean Modelling 152 (2020) 101644

Contents lists available at ScienceDirect

Ocean Modelling

journal homepage: www.elsevier.com/locate/ocemod

Three-dimensional time-optimal path planning in the ocean

Chinmay S. Kulkarni, Pierre F.J. Lermusiaux *

Department of Mechanical Engineering, Massachusetts Institute of Technology, 77 Mass. Ave., Cambridge, MA 02139, United States of America

ARTICLE INFO

Keywords:
Path planning
Three-dimensional
Level set
Data-assimilation
Ocean forecasting
AUVs
Gliders
Floats

ABSTRACT

Autonomous underwater vehicles (AUVs) operate in the three-dimensional and time-dependent marine environment with strong and dynamic currents. Our goal is to predict the time history of the optimal three-dimensional headings of these vehicles such that they reach the given destination location in the least amount of time, starting from a known initial position. We employ the exact differential equations for time-optimal path planning and develop theory and numerical schemes to accurately predict three-dimensional optimal paths for several classes of marine vehicles, respecting their specific propulsion constraints. We further show that the three-dimensional path planning problem can be reduced to a two-dimensional one if the motion of the vehicle is partially known, e.g. if the vertical component of the motion is forced. This reduces the computational cost. We then apply the developed theory in three-dimensional analytically known flow fields to verify the schemes, benchmark the accuracy, and demonstrate capabilities. Finally, we showcase time-optimal path planning in realistic data-assimilative ocean simulations for the Middle Atlantic Bight region, integrating the primitive-equation of the Multidisciplinary Simulation Estimation and Assimilation System (MSEAS) with the three-dimensional path planning equations for three common marine vehicles, namely propelled AUVs (with unrestricted motion), floats (that only propel vertically), and gliders (that often perform sinusoidal yo-yo motions in vertical planes). These results highlight the effects of dynamic three-dimensional multiscale ocean currents on the optimal paths, including the Gulf Stream, shelfbreak front jet, upper-layer jets, eddies, and wind-driven and tidal currents. They also showcase the need to utilize data-assimilative ocean forecasts for planning efficient autonomous missions, from optimal deployment and pick-up, to monitoring and adaptive data collection.

1. Introduction

The problem of planning feasible, safe, and optimal paths in complex and dynamic environments has received much attention from many branches of science and engineering. In the most general sense, 'optimal path planning' refers to a set of rules provided to an autonomous robot such that the robot can navigate from some initial configuration to the desired configuration in an optimal fashion. Typically, such optimality is governed by some objective function. Autonomous robotic platforms are becoming ubiquitous day by day, and are used to perform a variety of tasks with different levels of complexity. This leads to a wide range of objective functions. Principled path planning theories that apply to several situations are thus not common.

Optimal navigation of autonomous underwater vehicles (AUVs) is crucial for many applications, including security, search and rescue, monitoring, and data collection. Underwater gliders and floats are ideal for ocean sampling due to their long-range endurance and significant autonomy. However, these vehicles typically travel at relatively slow speeds, in many cases comparable to that of the local ocean currents (Schmidt et al., 1996; Elisseeff et al., 1999; Yan et al., 2014). Hence, the effect of currents on their net motion cannot be neglected and should be modeled accurately. The ocean environment in which these vehicles operate is however a highly dynamic system with high spatio-temporal variability (Cushman-Roisin and Beckers, 2011). It is therefore challenging to develop accurate and efficient methodologies to predict paths that optimize a desired objective function while modeling both the dynamic environment and the vehicle constraints. Achieving such principled path planning in three dimensions, integrating data-assimilative ocean modeling with model predictive control, is the motivation of the present work.

Existing works in underwater path planning have mostly studied two-dimensional (2D) or quasi-two-dimensional scenarios (Kulkarni, 2017). However, ocean currents often differ greatly with depth (Cushman-Roisin and Beckers, 2011). In order to reach the destination in optimal time, underwater vehicles need to utilize favorable currents and also avoid adverse currents by diving or rising to appropriate depths. Underwater path planning in fully three-dimensional (3D) real ocean domains is thus of great importance. Predicting ocean currents over real domains is needed for such planning but numerically

* Corresponding author.
E-mail addresses: chinmayk@mit.edu (C.S. Kulkarni), pierrel@mit.edu (P.F.J. Lermusiaux).

https://doi.org/10.1016/j.ocemod.2020.101644
Received 8 December 2019; Received in revised form 26 April 2020; Accepted 25 May 2020
Available online 17 June 2020

challenging. Oceans are complex dynamical systems, with multiple time-scales from seconds to years, and length-scales from millimeters to hundreds of kilometers (Cushman-Roisin and Beckers, 2011). Robust and accurate numerical schemes, and data assimilative models, are thus needed (Lermusiaux et al., 2006b; Lermusiaux et al., 2006; Pinardi et al., 2017). Further, there are different types of marine vehicles with specific degrees of freedom and propulsion constraints. Typical marine gliders used for sampling data commonly perform a sinusoidal motion (Rudnick et al., 2004; Testor et al., 2010; Javaid et al., 2014) whereas floats that drift with ocean currents are only able to perform vertical motion by adjusting their buoyancy (Roemmich et al., 2009; Kobayashi et al., 2012). In order to plan feasible, safe, and optimal trajectories for such vehicles, one needs to respect these specific propulsion constraints. The desired attributes listed above are crucial to optimal path planning in real ocean scenarios.

In the present work, we start from the governing path planning equations (Lolla et al., 2012, 2014a,b; Lermusiaux et al., 2016). They account for the effects of the dynamic environmental flow field on the net vehicle motion. They predict exact globally optimal paths without heuristics (Lolla and Lermusiaux, 2020), are computationally efficient (Lolla et al., 2012), and can account for unsafe/forbidden regions and stationary or moving obstacles (Lolla et al., 2015). The effectiveness of the algorithms was experimentally demonstrated in multiple sea-trials (Subramani et al., 2017b; Edwards et al., 2017; Mirabito et al., 2017). Results were extended to predict the paths that minimize the energy usage (Subramani and Lermusiaux, 2016; Subramani et al., 2017a) or maximize the quality of data collected by the vehicles (Lolla, 2016; Lermusiaux et al., 2017). Presently, for the first time, we address both fully 3D realistic ocean setups and 3D propulsion constraints. We develop the theory and numerical methods to handle the complexities of dynamic 3D flow fields and motion constraints on realistic marine vehicles. We verify the schemes in benchmark flows. We then analyze results in the Middle Atlantic Bight region. We describe the regional dynamics and our data-assimilative ocean modeling system. We finally showcase the impact of the dynamic 3D circulation features on the evolution of the reachability fronts and time-optimal paths for several common types of marine vehicles.

The paper is organized as follows. We first briefly review prior results on 3D path planning in static and dynamic environments. In Section 2, we state the problem and provide the equations that govern the optimal trajectories. Extensions to motion-constrained marine vehicles in 3D domains are derived in Section 3. In Section 4, we develop numerical schemes to achieve high accuracy in real ocean domains. In Section 5, we verify the path planning in 3D analytical benchmark flows. In Section 6, we describe the dynamics and modeling of the Middle Atlantic Bight region, and complete realistic simulations to compare and contrast path planning for common types of marine vehicles. The summary and conclusions are in Section 7.

1.1. Prior progress in optimal path planning in three-dimensional and realistic domains

Optimal path planning in 3D domains is a complex and challenging problem, and hence algorithms for the same have not been studied extensively. However, utilizing environmental flows and planning feasible (although sub-optimal) paths in three-dimensions has been elaborately studied by several researchers from a wide variety of areas. For example, Kiraly et al. (2004) compute feasible 3D trajectories for a bronchoscope in various airways inside the human body while Siddon (1985) plans paths for 3D computed tomography in radiology.

Nature also serves as a motivation for optimal planning problems. For example, Richardson (2012) and Sachs et al. (2013) mimic the dynamic soaring of the Albatross for autonomous aerial vehicles in order to optimize energy consumption. The Albatross utilizes the lee eddies located downwind of sharp-crested waves to increase its speed. Such a maneuver requires minor adjustments to the trajectory but saves significant energy. Other similar dynamic soaring patterns to minimize the energy spent during travel are also studied by Bonnin (2016) and Zhao (2004).

Planning feasible and collision-free trajectories for aerial vehicles is an active field, with many established approaches. Lozano-Pérez and Wesley (1979) use a network-based scheme to plan paths in domains with forbidden regions and obstacles. Mittal and Deb (2007) attempt to plan feasible paths offline using evolutionary algorithms. Wong and Fu (1986) utilize a network-based scheme on two-dimensional sections of the 3D domain for computational efficiency. This idea of planning collision-free paths is also extended to larger aircraft and congested airports, for which most results rely on optimization techniques such as integer programming. For example, Richards and How (2002) use mixed integer linear programming to plan collision-free aircraft trajectories, whereas Frazzoli et al. (2001) utilize semi-definite programming. Prete and Mitchell (2004) and Krozel et al. (2006) employ network-based approaches to compute safe aircraft trajectories that minimize travel in time-varying 3D hazardous weather regions.

In the ocean domain, Pereira et al. (2013) provide an algorithm to compute 3D underwater vehicle paths that minimize the risk of collision with ships and land. They use the Regional Ocean Modeling System for oceanic flow fields and a Markov-decision-process-based approach and expectation–minimization to decrease the risk of collision. Smith et al. (2010) further extend this methodology to tracking a dynamically evolving ocean feature while minimizing the risk of collision with ships and other possible obstacles. Petillot et al. (2001) utilize data from an onboard sonar sensor to plan paths that minimize the risk of collisions with objects and obstacles in the ocean.

A common approach towards optimal path planning is to use a myopic optimization, where the vehicle chooses the short-term optimal option among other options. Global optimality is then not guaranteed, but the approach is nonetheless useful. For example, Zamuda and Sosa (2014) consider a glider that gathers data while following a path towards some set destination where a short-term opportunistic sampling algorithm is used to maximize the quality of the data collected. A continuum viewpoint has also been used for 3D robotic path planning such as the potential field method, eliminating the need for network-based models (Connolly et al., 1990; Wang and Chirikjian, 2000). All obstacles are then assumed to exert a repelling force whereas the target position exerts an attractive force on a potential function. Heuristics are needed to account for the effect of external flow fields on the computed path.

Finally, to plan glider paths in 3D ocean environments, Garau et al. (2014) used the A* algorithm (Hart et al., 1968) with examples in the western Mediterranean sea. Even though the A* algorithm is efficient, its use of heuristics does not guarantee global optimality. Witt and Dunbabin (2008) build upon Kruger et al. (2007) to find paths that minimize the energy spent by an autonomous vehicle in 3D ocean domains. This is achieved by using the present current to the greatest advantage. This local method efficiently chooses an energy optimal path amongst the considered candidate paths. However, as all the possible paths are not considered, strict global optimality is not ensured. For more extensive reviews, we refer to Kulkarni (2017).

2. Optimal path planning using the level set method: Theory

In what follows, we formally describe the problem statement and introduce the exact time-optimal path planning equations that establish the theoretical foundation. Further details can be found in Lolla et al. (2014b), Lolla (2016) and Lolla and Lermusiaux (2020).

2.1. Problem statement

Consider the motion of a vehicle from the start point ($\mathbf{x}_s$) to the destination ($\mathbf{x}_f$) in the domain $\Omega \subseteq \mathbb{R}^3$. Let the trajectory of the vehicle be given by $\mathbf{X}(t)$. Fig. 1 illustrates the velocity components of

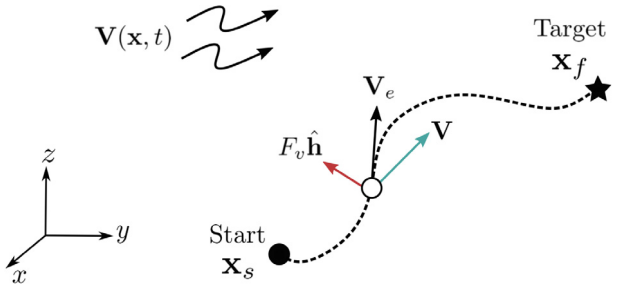

Fig. 1. The vehicle, at position $\mathbf{x}$ at some time t, experiences the external velocity $\mathbf{V}(\mathbf{x},t)$, e.g. the ocean currents (cyan arrow), and steers itself along chosen heading $\hat{\mathbf{h}}(t)$ with speed $F_v(\hat{\mathbf{h}},t)$ (red arrow). The net effective velocity V_e of the vehicle is the vector sum of the advective velocity field ($\mathbf{V}$) and the steering propulsion of the vehicle ($F_v\hat{\mathbf{h}}$).

the vehicle as it moves from the start point to the target. The first component is the vehicle propulsion in the direction of the heading $\hat{\mathbf{h}}$ with a speed F_v, that is bounded by zero and a maximum speed, i.e. $0 \leq F_v \leq F(\hat{\mathbf{h}},\mathbf{X},t)$. This latter *maximum* nominal propulsion speed of the vehicle, denoted by $F(\hat{\mathbf{h}},\mathbf{x},t)$, is in general a given function of the heading direction ($\hat{\mathbf{h}}$), spatial location ($\mathbf{x}$), and present time (t). The vehicle is also forced by a dynamic external velocity field $\mathbf{V}(\mathbf{x},t) : \Omega \times [0,\infty) \to \mathbb{R}^3$. The second velocity component of vehicle is thus the advection by the velocity field $\mathbf{V}(\mathbf{X}(t),t)$, i.e. the ocean currents.

The effective velocity experienced by the vehicle is given by,

$$\mathbf{V}_e(\mathbf{X}(t),t) = \frac{d\mathbf{X}(t)}{dt} = (F_v\hat{\mathbf{h}} + \mathbf{V}(\mathbf{X}(t),t)). \tag{1}$$

In nautical jargon, the magnitude of the horizontal component of the effective velocity ($\mathbf{V}_e$) is often referred to as 'speed over ground' and the vehicle speed F_v as 'speed through water'. We denote the 'first arrival time' function by $T(\mathbf{x} : \mathbf{x}_0, t_0)$: it is the time at which the vehicle reaches any specified point $\mathbf{x}$ for the first time, given that it started from $\mathbf{x}_0$ at time t_0. Clearly, we have,

$$T(\mathbf{x}_s : \mathbf{x}_s, 0) = 0 \quad \text{and} \quad \mathbf{X}(T(\mathbf{x}_f : \mathbf{x}_s, 0)) = \mathbf{x}_f. \tag{2}$$

It is proven that in order for the vehicle to reach the desired destination in the minimum amount of time, it must travel at the maximum allowable speed (Lolla and Lermusiaux, 2020; Lolla, 2016). We thus wish to compute the vehicle heading ($\hat{\mathbf{h}}$) as a function of time that yield minimum travel time for the vehicle between $\mathbf{x}_s$ and $\mathbf{x}_f$, subject to the constraints imposed by Eqs. (1) and (2). Hence, we search for $\hat{\mathbf{h}}(t)_{optimal}$ defined by,

$$\hat{\mathbf{h}}(t)_{optimal} = \arg\min_{\hat{\mathbf{h}},F_v} T(\mathbf{x}_f : \mathbf{x}_s, 0). \tag{3}$$

Note that in the above formulation, the optimal heading choice $\hat{\mathbf{h}}(t)_{optimal}$ is also a function of the position of the vehicle along the optimal trajectory, *i.e.* $\mathbf{X}(t)$. However, as this position itself is function of time (once the optimal path is known), we drop this implicit dependency of $\hat{\mathbf{h}}(t)_{optimal}$ on $\mathbf{X}(t)$.

2.2. Approach

Exact time-optimal path planning hinges upon the concept of reachability (Lolla, 2016). The reachable set is the set of *all the points* that can be visited by the vehicle by the considered time, given the starting point of the vehicle. At any time, all the points that lie on the boundary of the reachable set, i.e. the reachability front, have been reached for the first time: the value of their first arrival time function is the present time.

By keeping track of the reachability front at all times one can determine the time when this front reaches the target for the first time, which is the minimum travel time between the start position and the target. A path traced by a point that always travels on the reachability front and reaches the target is exactly an optimal path we wish to compute (note that there can be multiple optimal paths). This broadly divides the problem in two sub-parts: (i) first, the forward evolution of the reachable set and front, and (ii) second, once the reachability front reaches the destination, the optimal trajectory traced backwards in time. We refer to these sub-parts as 'forward evolution of the reachable set' and 'backward tracing of the optimal path', respectively. Fig. 2 pictorially depicts the reachability front (analogous to a first wave front), and the possible heading choices at two different positions. This two step approach involving the forward evolution of the reachability front followed by backward tracing of the optimal trajectory (which is a characteristic passing through the destination of the PDE governing the reachability front evolution) has been proven to be exact, even when the external flow speed is larger than the vehicle speed (*i.e.* the vehicle is not fully controllable) (Lolla, 2016; Lolla and Lermusiaux, 2020).

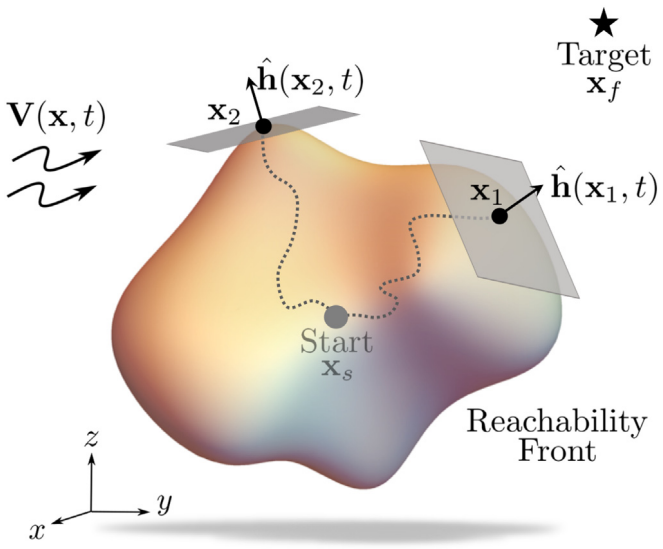

Fig. 2. Evolution of the reachability front in 3 dimensions. Two sample positions ($\mathbf{x}_1$ and $\mathbf{x}_2$) and headings at these positions are illustrated (tangent planes to the reachability front at these positions shown for reference). The dashed lines sketch the trajectories (within the reachable set) that optimal particles follow to reach $\mathbf{x}_1$ and $\mathbf{x}_2$.

2.3. Forward evolution of the reachable set and backward tracing of the optimal path

We use the level set method to predict the propagation of the reachability front. The front is then embedded as the zero level set of a signed distance function (henceforth denoted by $\boldsymbol{\phi}$). The zero level set of a function is simply the set of points at which the function value is zero. It is evolved until the target lies on it. Once this is achieved, we compute the optimal path by tracing the trajectory of the particle that always traveled on the reachability front and reached the target at the first arrival time. This is done by solving the particle motion ODE Eq. (1) backward in time starting from the destination, and by utilizing the optimal heading information from the reachable set evolution.

In general, we have two free control parameters, namely the vehicle speed (F_v) and the vehicle heading ($\hat{\mathbf{h}}$). We would like to predict the optimal values of these control parameters (as a function of time) such that the first arrival time function for the target point $T(\mathbf{x}_f : \mathbf{x}_s, t_0)$ is minimized. It is proven that, for the vehicle to reach the desired destination in the minimum amount of time, it must travel at the maximum allowable speed (Lolla and Lermusiaux, 2020; Lolla, 2016). This implies that the only control parameter is the heading of the vehicle. We now simply state the significant results that express the solution of this minimization problem. More details regarding the same

may be found in Appendix A and Lolla and Lermusiaux (2020), Lolla (2016).

We assume that the possible vehicle trajectories $\mathbf{X}(t)$ are governed by Eq. (1), with initial condition $\mathbf{X}(0) = \mathbf{x}_s$. Then, the evolution of the reachability front is given by the zero level set of the function $\boldsymbol{\phi}$, where $\boldsymbol{\phi}(\mathbf{x}, t)$ is the unique viscosity solution (Osher and Fedkiw, 2006; Lolla and Lermusiaux, 2020) of the following the Hamilton–Jacobi level set equation,

$$\frac{\partial \boldsymbol{\phi}(\mathbf{x},t)}{\partial t} + \max_{\hat{\mathbf{h}}(\mathbf{x},t)} \left(F(\hat{\mathbf{h}},\mathbf{x},t)\,\hat{\mathbf{h}}(\mathbf{x},t)\cdot\nabla\boldsymbol{\phi}\right) + \mathbf{V}(\mathbf{x},t)\cdot\nabla\boldsymbol{\phi}(\mathbf{x},t) = 0\,, \tag{4}$$

with the initial conditions,

$$\boldsymbol{\phi}(\mathbf{x},0) = |\mathbf{x}-\mathbf{x}_s|. \tag{5}$$

The second term on the left hand side of Eq. (4) incorporates the propulsion of vehicles, and is referred to as the 'optimal propulsion term'. The last term on the left hand side of Eq. (4) is referred to as the 'advection term', as it accounts for the transport of the vehicle by the background external velocity field, i.e. the predicted ocean currents. In what follows, for clarity, we do not explicitly retain the functional dependencies of $\boldsymbol{\phi}$, $\hat{\mathbf{h}}$, and $\mathbf{V}$ on $(\mathbf{x}, t)$, and of F on $(\hat{\mathbf{h}}, \mathbf{x}, t)$, unless there is a specific need to clearly denote these dependencies or when it helps in understanding.

In the special case when the vehicle speed $F(\hat{\mathbf{h}}, \mathbf{x}, t)$ is independent of the heading $\hat{\mathbf{h}}$ of the vehicle (isotropic speed), the maximization can be performed analytically. The resulting Hamilton–Jacobi level set equation for this case is given by Eq. (6):

$$\frac{\partial \boldsymbol{\phi}}{\partial t} + F(\mathbf{x},t)\,|\nabla\boldsymbol{\phi}| + \mathbf{V}\cdot\nabla\boldsymbol{\phi} = 0\,, \tag{6}$$

We solve Eq. (4) until the target $(\mathbf{x}_f)$ lies on or just inside the reachability front (*i.e.* until $\boldsymbol{\phi}(\mathbf{x}_f, t) \leq 0$). Once this is achieved, the optimal trajectory (or trajectories) $\mathbf{X}(t)$ is given by the characteristic lines of Eq. (4). That is, $\mathbf{X}(t)$ satisfies the following equation,

$$\begin{aligned} &\frac{d\mathbf{X}(t)}{dt} = F(\hat{\mathbf{h}},\mathbf{X},t)\hat{\mathbf{h}}(t) + \mathbf{V}(\mathbf{X},t) \qquad \text{where} \\ &\hat{\mathbf{h}}(t) = \arg\max_{\hat{\mathbf{h}}(\mathbf{X},t)} \left(F(\hat{\mathbf{h}},\mathbf{X},t)\,\hat{\mathbf{h}}(\mathbf{X},t)\cdot\nabla\boldsymbol{\phi}(\mathbf{X},t)\right). \end{aligned} \tag{7}$$

These 3D governing path planning equations are exact. It is only when they are numerically integrated that truncation/round-off errors are made, and with fine enough resolutions, these errors go to zero. This is a major advantage when compared to planning schemes that are inexact due to heuristics or simplifications, or that are too expensive. Of course, all these schemes also make numerical errors once implemented on a computer (e.g. for graph methods, errors depend on graph resolution, connectivity, time-step, etc., see Mannarini et al. (2020)).

3. Modeling of realistic marine vehicles

We now extend the theory to motion-constrained vehicles in 3D domains, capturing the behavior of commonly used marine vehicles. First, we treat vehicles whose speed depends on their heading direction. Such vehicles are referred to as 'vehicles with anisotropic speeds'. Vehicles that are constrained to move only along certain directions may also be included in this category, as it can be assumed that the vehicle speed is non-zero only along the permitted direction(s) of travel. The second class considers vehicles whose motion is known partially. In general, this motion is assumed to be known along a specific direction (which itself could be a function of time). We refer to such vehicles as 'vehicles with partially known motion'.

3.1. Vehicles with anisotropic speeds

The reachability front is governed by Eq. (4), where it is embedded as the zero level set of the level set function $\boldsymbol{\phi}$. If the propulsion speed of the vehicle is dependent on its heading direction, a maximization over all the heading directions is required to be performed at each point of the front (or domain) at all times to evaluate the optimal propulsion term. Details of the same are discussed in Appendix B.

If the expression for vehicle speed F is known in terms of the heading $\hat{\mathbf{h}}$ (and the time t), then the maximization may be performed analytically. As an example, we consider the case of an oceanic float. These vehicles can only propel in the vertical direction by adjusting their buoyancy (Rudnick et al., 2004), and are advected by the environmental flow, mostly in the horizontal due to the commonly smaller ocean vertical currents. We model this by enforcing the following:

$$\hat{\mathbf{h}} \in \mathcal{H}_z = \{\hat{\mathbf{n}}_z, -\hat{\mathbf{n}}_z, 0\} \tag{8}$$

where $\mathcal{H}_z$ is a subset of $\mathbb{R}^3$ and $\hat{\mathbf{n}}_z = (0,0,1)$ is the unit vector along the vertical (Z) direction. Eq. (8) implies that the only directions that the vehicle can be steered in are vertically up or vertically down. Using this in the maximization term, we obtain,

$$\begin{aligned} \max_{\hat{\mathbf{h}}(\mathbf{x},t)} \left(F(\hat{\mathbf{h}},\mathbf{x},t)\,\hat{\mathbf{h}}(\mathbf{x},t)\cdot\nabla\boldsymbol{\phi}(\mathbf{x},t)\right) &= F\left(\max\left((0,0,\pm1)\cdot\left(\boldsymbol{\phi}_x,\boldsymbol{\phi}_y,\boldsymbol{\phi}_z\right)\right)\right) \\ &= F\left(\max\left(\pm\boldsymbol{\phi}_z\right)\right) \\ &= F\left|\frac{\partial\boldsymbol{\phi}(\mathbf{x},t)}{\partial z}\right|. \end{aligned} \tag{9}$$

Substituting this result in Eq. (4), the final Hamilton–Jacobi equation to be solved for the motion of a float is given by,

$$\frac{\partial\boldsymbol{\phi}}{\partial t} + F\left|\frac{\partial\boldsymbol{\phi}}{\partial z}\right| + \mathbf{V}\cdot\nabla\boldsymbol{\phi} = 0\,, \tag{10}$$

with all the possible optimal headings on the reachability front given by,

$$\hat{\mathbf{h}}(\mathbf{x},t) = sign\left(\frac{\partial\boldsymbol{\phi}(\mathbf{x},t)}{\partial z}\right)\hat{\mathbf{n}}_z. \tag{11}$$

The optimal floats headings thus depend on the flow field implicitly through $\boldsymbol{\phi}(\mathbf{x}, t)$. A float that first reaches the target $\mathbf{x}_f$ will thus alter its upward or downward motion according to the sign of the vertical gradient of $\boldsymbol{\phi}(\mathbf{x}, t)$ along the optimal trajectory governed by Eq. (7).

3.2. Vehicles with partially known motion

We now examine vehicles whose motion is known along some (time-dependent) direction. We prove that in such cases, the 3D problem can be decomposed into a two-dimensional problem with a 'hybrid' velocity field, yielding significant computational savings (as will be seen in Sections 4, 5, and 6).

Let us assume that the motion of the vehicle at a location $\mathbf{x}$ and time t is known along some direction $\hat{\mathbf{n}}(\mathbf{x}, t)$. Let the maximum propulsion speed of the vehicle along $\hat{\mathbf{n}}(\mathbf{x}, t)$ be $F_n(\mathbf{x}, t)$, also assumed to be known. Let the heading of the vehicle in the plane orthogonal to $\hat{\mathbf{n}}(\mathbf{x}, t)$ at position $\mathbf{x}$ and time t be $\hat{\mathbf{h}}_\perp(\mathbf{x}, t)$ with speed $F_\perp(\hat{\mathbf{h}}_\perp, \mathbf{x}, t) = \left(F(\hat{\mathbf{h}},\mathbf{x},t)^2 - F_n(\mathbf{x},t)^2\right)^{\frac{1}{2}}$. In what follows, for clarity, we drop the dependencies of $\boldsymbol{\phi}$, $\mathbf{V}$, $\hat{\mathbf{n}}$, and F_n on $(\mathbf{x}, t)$ and of $F_\perp$ on $(\hat{\mathbf{h}}_\perp, \mathbf{x}, t)$. Note that F_n cannot be a function of $\hat{\mathbf{h}}_\perp$ as that implies that the component subproblems cannot be decoupled, as will be seen. However, as F depends on $\hat{\mathbf{h}}$, the resulting $F_\perp$ is also a function of $\hat{\mathbf{h}}$. Since $\hat{\mathbf{h}}$ is the unit vector in the direction $\hat{\mathbf{h}}_\perp + \hat{\mathbf{n}}$, where $\hat{\mathbf{n}}$ is known at all locations at all times and cannot be optimized, we can nonetheless reduce the dependency of $F_\perp$ on $\hat{\mathbf{h}}$ to a dependency on $\hat{\mathbf{h}}_\perp$ only. The Hamilton–Jacobi equation (4) can thus be written as,

$$\begin{aligned} &\frac{\partial\boldsymbol{\phi}}{\partial t} + \max_{\hat{\mathbf{h}}_\perp}\left(\left(F_n\hat{\mathbf{n}} + F_\perp\hat{\mathbf{h}}_\perp\right)\cdot\nabla\boldsymbol{\phi}\right) + \mathbf{V}\cdot\nabla\boldsymbol{\phi} = 0\,, \\ \Leftrightarrow\ &\frac{\partial\boldsymbol{\phi}}{\partial t} + \max_{\hat{\mathbf{h}}_\perp}\left(F_\perp\hat{\mathbf{h}}_\perp\cdot\nabla\boldsymbol{\phi}\right) + \left(\mathbf{V} + F_n\hat{\mathbf{n}}\right)\cdot\nabla\boldsymbol{\phi} = 0\,. \end{aligned} \tag{12}$$

The advective velocity field itself can be written in terms of component along $\hat{\mathbf{n}}(t)$ and components orthogonal to $\hat{\mathbf{n}}(t)$. Let us denote this decomposition of the velocity field as,

$$\mathbf{V}(\mathbf{x},t) = V_n(\mathbf{x},t)\,\hat{\mathbf{n}}(\mathbf{x},t) + V_\perp(\mathbf{x},t)\,\hat{\mathbf{n}}_\perp(\mathbf{x},t)\,, \tag{13}$$

Table 1
Scales for non-dimensionalization.

Variable	Scale
x	$x^c = L_x$ (Characteristic length in the X direction)
y	$y^c = L_y$ (Characteristic length in the Y direction)
z	$z^c = L_z$ (Characteristic length in the Z direction)
V_x	$V_x^c = \text{mean}_{\mathbf{x},t}(V_x(\mathbf{x},t))$
V_y	$V_y^c = \text{mean}_{\mathbf{x},t}(V_y(\mathbf{x},t))$
V_z	$V_z^c = \text{mean}_{\mathbf{x},t}(V_z(\mathbf{x},t))$
t	$t^c = \max\left(\frac{\lvert x_f - x_s\rvert}{\max(V_x^c, F_x^{\max})}, \frac{\lvert y_f - y_s\rvert}{\max(V_y^c, F_y^{\max})}, \frac{\lvert z_f - z_s\rvert}{\max(V_z^c, F_z^{\max})}\right)$

where $\hat{\mathbf{n}}_\perp(\mathbf{x},t)$ denotes the basis of the plane orthogonal to $\hat{\mathbf{n}}(\mathbf{x},t)$ and $\mathbf{V}_\perp(\mathbf{x},t) = V_\perp(\mathbf{x},t)\ \hat{\mathbf{n}}_\perp(\mathbf{x},t)$ is the corresponding velocity component. Substituting this in Eq. (12), we obtain,

$$\frac{\partial \boldsymbol{\phi}}{\partial t} + \max_{\hat{\mathbf{h}}_\perp}\left(F_\perp \hat{\mathbf{h}}_\perp \cdot \nabla\boldsymbol{\phi}\right) + \left(V_\perp \hat{\mathbf{n}}_\perp + \left(V_n + F_n\right)\hat{\mathbf{n}}\right)\cdot\nabla\boldsymbol{\phi} = 0\,. \tag{14}$$

We will next use a 1st order operator splitting (fractional step) method (Wheeler and Dawson, 1987; Ferziger et al., 2020) to split Eq. (14) into two constituent equations. The first equation describes the evolution of the projection of $\boldsymbol{\phi}$ onto $\hat{\mathbf{n}}_\perp$, $\boldsymbol{\phi}_\perp$, and the second describes the evolution of $\boldsymbol{\phi}$ along $\hat{\mathbf{n}}$, $\boldsymbol{\phi}_n$. Together, the sum of these two contributions yields the evolution of $\boldsymbol{\phi}$ in Ω if their full coupling is maintained, as is seen in the following:

$$\frac{\partial \boldsymbol{\phi}_\perp}{\partial t} + \max_{\hat{\mathbf{h}}_\perp}\left(F_\perp \hat{\mathbf{h}}_\perp \cdot \nabla\boldsymbol{\phi}\right) + V_\perp \hat{\mathbf{n}}_\perp \cdot \nabla\boldsymbol{\phi} = 0\,, \tag{15a}$$

$$\frac{\partial \boldsymbol{\phi}_n}{\partial t} + \left(V_n + F_n\right)\hat{\mathbf{n}}\cdot\nabla\boldsymbol{\phi} = 0\,, \tag{15b}$$

$$\Rightarrow \frac{\partial \boldsymbol{\phi}}{\partial t} = \frac{\partial \boldsymbol{\phi}_\perp}{\partial t} + \frac{\partial \boldsymbol{\phi}_n}{\partial t}\,. \tag{15c}$$

Eq. (15a) represents the evolution of the reachable set in the plane orthogonal to $\hat{\mathbf{n}}(t)$, whereas Eq. (15b) represents the contribution due to the advective and vehicle motion along $\hat{\mathbf{n}}(t)$, which does not require any optimization. Hence, in this case, the only optimal control problem to be solved is represented by Eq. (15a), which is a reachable set evolution in two dimensions. The contribution due to Eq. (15b) is then locally added in order to obtain the final value of $\partial\boldsymbol{\phi}/\partial t$ by summation. The initial conditions are, for Eq. (15a), $\boldsymbol{\phi}_\perp(\mathbf{x},0) = |(\mathbf{x})_\perp - (\mathbf{x}_s)_\perp|$, and for Eq. (15b), $\boldsymbol{\phi}_n(\mathbf{x},0) = |(\mathbf{x})_n - (\mathbf{x}_s)_n|$, where the subscripts $\perp$ and n then indicate projection orthogonal to and along $\hat{\mathbf{n}}(0)$, respectively.

As for the forward evolution, the backward trajectory of the vehicle also consists of two parts: (i) the motion in the orthogonal plane $\hat{\mathbf{n}}_\perp(t)$ and (ii) the component along $\hat{\mathbf{n}}(t)$. Thus the ODE defining the optimal trajectory also consists of the sum of two corresponding components,

$$\frac{d\mathbf{X}_\perp}{dt} = F_\perp \hat{\mathbf{h}}_\perp + \mathbf{V}_\perp\,, \tag{16a}$$

$$\frac{d\mathbf{X}_n}{dt} = F_n \hat{\mathbf{n}}\,, \tag{16b}$$

$$\frac{d\mathbf{X}}{dt} = \frac{d\mathbf{X}_\perp}{dt} + \frac{d\mathbf{X}_n}{dt}\,. \tag{16c}$$

where $\hat{\mathbf{h}}_\perp(t) = \arg\max_{\hat{\mathbf{h}}_\perp(\mathbf{X},t)}\left(F_\perp(\hat{\mathbf{h}}_\perp,\mathbf{X},t)\,\hat{\mathbf{h}}_\perp(\mathbf{X},t)\cdot\nabla\boldsymbol{\phi}(\mathbf{X},t)\right)$. Eq. (16a) represents the optimal trajectory orthogonal to $\hat{\mathbf{n}}(t)$ while Eq. (16b) governs the path along $\hat{\mathbf{n}}(t)$. As with Eq. (7), Eq. (16c) is solved in backward time, starting from $\mathbf{X}\left(T\left(\mathbf{x}_f : \mathbf{x}_s, 0\right)\right) = \mathbf{x}_f$ to compute the optimal trajectory.

Numerically, if Eqs. (15a) and (15b) are integrated separately over Δt without coupling between them, splitting errors are made. The same can be said about the split backward tracing equations (16). These numerical issues are discussed in Section 4.5.

4. Numerical schemes for realistic ocean domains

We now develop accurate, consistent, and efficient numerical schemes for the path planning equations. We first present challenges in realistic 3D ocean scenarios and obtain the non-dimensional form of the Hamilton–Jacobi level set equation which is crucial in solving underwater path planning problems. We then emphasize the advantages of numerical consistency between the discrete forward evolution of the reachable set and discrete backward tracing of the optimal path. Finally, we develop high-order spatial and temporal numerical schemes for the forward evolution of the zero level set function and novel implicit schemes for the backward tracing of the optimal path.

4.1. Challenges in real ocean domains and non-dimensionalization of the Hamilton–Jacobi equation

Most stratified geophysical fluid flows are extremely anisotropic in terms of length and/or velocity scales, with orders of magnitude difference between the horizontal and vertical scales (Cushman-Roisin and Beckers, 2011). Such disparity in the length scales (e.g. horizontal scales of kilometers and vertical scales of meters) significantly affects simulations of 3D oceanic domains, where even small deviations in some direction may cause large changes in the other directions. In many ocean prediction models, the vertical velocity is obtained as a diagnostic variable. For example, in hydrostatic models, one computes the vertical flow velocity by enforcing the divergence-free condition and accounting for the free surface motion (Haley Jr. and Lermusiaux, 2010). These vertical velocities, e.g., $\mathcal{O}(10^{-3}$ cm/s to 10^{-1} cm/s), are typically much smaller in magnitude than horizontal ones, e.g., $\mathcal{O}$(1 cm/s to 1 m/s). This implies that the vertical advective fluxes may be severely altered even by small relative errors in the fluxes in other directions, thus impacting the accuracy of the zero level set evolution in three dimensions. To ensure that such a discrepancy in scales does not affect the fidelity of the computation, we non-dimensionalize the Hamilton–Jacobi level set equation (4),

To non-dimensionalize, a reference scale needs to be set up for each of the variables. For each of the spatial dimensions and each of the corresponding velocity components, one commonly utilizes a characteristic length (e.g. domain length) and velocity magnitude. The other variables that remain are the level set function $\boldsymbol{\phi}$ and the time t. The non-dimensionalizing scales that we propose are summarized in Table 1. The characteristic scales for the velocities are averages over the entire spatial and temporal domain of interest, and are computed only once per simulation. Another suitable scale for velocities could also be the maximum velocity in that direction over the entire temporal domain of interest. Although an acceptable choice, the maximum velocity can be much larger than the typical expected velocity magnitudes, and the non-dimensionalization would then not be very effective in such cases. If the velocities in different regions vary greatly, then the domain can be divided into appropriate sub-domains and a separate non-dimensional scale for the velocities can also be chosen in each of the domains. The characteristic time scale used is an estimate for the travel time assuming that the vehicle either travels only at its own speed or is only advected with the flow, whichever is the faster choice. Specifically, we look at the maximum of the travel times along each of the basis directions (that is, along the X, Y and Y directions) when the vehicle optimally chooses to either travel with the flow, or travel on its own, but not both. It must be stated that these choices are far from unique, and appropriate characteristic scales should be chosen based on the specifics of the problem. No scale for $\boldsymbol{\phi}$ is required as the partial differential equation (PDE) is linear in $\boldsymbol{\phi}$ and independent of the scaling of $\boldsymbol{\phi}$.

The numerically well-conditioned non-dimensional form of Eq. (4) is given by Eq. (17), where the superscript $(\bullet^*)$ refers to the non-dimensional quantity corresponding to $(\bullet)$,

$$\frac{1}{t^c}\frac{\partial \boldsymbol{\phi}^*}{\partial t^*} + \max_{\hat{h}_x,\hat{h}_y,\hat{h}_z}\left(F\left(\frac{\hat{h}_x(t)}{L_x}\frac{\partial \boldsymbol{\phi}^*}{\partial x^*} + \frac{\hat{h}_y(t)}{L_y}\frac{\partial \boldsymbol{\phi}^*}{\partial y^*} + \frac{\hat{h}_z(t)}{L_z}\frac{\partial \boldsymbol{\phi}^*}{\partial z^*}\right)\right) + \left(\frac{V_x^c}{L_x}V_x^*\frac{\partial \boldsymbol{\phi}^*}{\partial x^*} + \frac{V_y^c}{L_y}V_y^*\frac{\partial \boldsymbol{\phi}^*}{\partial y^*} + \frac{V_z^c}{L_z}V_z^*\frac{\partial \boldsymbol{\phi}^*}{\partial z^*}\right) = 0\,. \tag{17}$$

For the case of isotropic propulsion, this Eq. (17) reduces to

$$\frac{1}{t^c}\frac{\partial \boldsymbol{\phi}^*}{\partial t^*} + F\sqrt{\frac{1}{(L_x)^2}\left(\frac{\partial \boldsymbol{\phi}^*}{\partial x^*}\right)^2 + \frac{1}{(L_y)^2}\left(\frac{\partial \boldsymbol{\phi}^*}{\partial y^*}\right)^2 + \frac{1}{(L_z)^2}\left(\frac{\partial \boldsymbol{\phi}^*}{\partial z^*}\right)^2} + \left(\frac{V_x^c}{L_x}V_x^*\frac{\partial \boldsymbol{\phi}^*}{\partial x^*} + \frac{V_y^c}{L_y}V_y^*\frac{\partial \boldsymbol{\phi}^*}{\partial y^*} + \frac{V_z^c}{L_z}V_z^*\frac{\partial \boldsymbol{\phi}^*}{\partial z^*}\right) = 0\,. \tag{18}$$

The advective fluxes in each direction scale with the ratio $\frac{V}{L}$ in the corresponding direction. As is well known from mass conservation, even though both V_z and L_z are much smaller than either of V_x and L_x or V_y and L_y, the ratio $\frac{V_z}{L_z}$ can easily be comparable to $\frac{V_x}{L_x}$ and $\frac{V_y}{L_y}$. This means that even though the length and the velocity in the Z direction are small, the advection contribution in this direction may not be negligible. The contributions due to each of the directional terms in the optimal propulsion term scale as $\frac{1}{L_x}$, $\frac{1}{L_y}$, and $\frac{1}{L_z}$ in Eq. (17). This again implies that even though length of the domain in the Z direction is much smaller, the contribution to the optimal propulsion term in this direction can be substantial, even if the vertical propulsion speed is smaller than the horizontal one (anisotropic propulsion). Hence, ignoring or not completely resolving the motion in the vertical direction may cause large errors, as its contributions to both the optimal propulsion and advection are comparable to the other horizontal terms.

4.2. Numerical consistency between the forward evolution and backward tracking

A consideration in the computation of the optimal path is the numerical consistency between the discrete forward evolution and backward tracing. The forward reachability evolution is governed by the PDE (4). It represents the motion of all hypothetical 'optimal' points that could reach the destination through a functional representation of the reachability front in space. This PDE is often solved using explicit numerical time integration. Backward tracing of the optimal involves an ODE (7) that governs the spatial motion of an optimal point over time. For consistent (minimal) numerical errors, during discrete backtracking, we should match the discrete forward reachability front, i.e. exactly reverse the steps of the discrete forward time-integration. We then ensure that the optimal point numerically gets back to the start point. Specifically, we should maintain three numerical consistencies: forward/backward explicit/implicit time consistency, type of time-integration consistency, and spatial discretization consistency. For example, if the forward temporal evolution is explicit, then the backward temporal evolution should be implicit, and vice versa. The exact type of the forward evolution scheme also needs to be 'mimicked' by the backtracking scheme. For example, if the forward evolution uses the forward Euler time marching, then the backward tracing should use the backward Euler scheme. Finally, numerical consistency in space should also be maintained between the PDE and ODE, e.g. for the normals to the level set. If these consistencies are not maintained, the discrete local forward front and backward path integration do not exactly reverse numerically: with compounding of errors during the backtracking, we can then not guarantee getting back to the start point. Fig. 3 schematically represents the discrepancy arising during one time-step if numerical consistencies are not maintained. As it is much easier to solve a PDE through explicit time marching, we use implicit time marching for the backward tracing of optimal path, and hence an iterative solver is necessary for the ODE.

4.3. Numerical schemes: Forward evolution

The main interest is the accuracy of motion of the zero level of the level set function $\boldsymbol{\phi}$. Small deviations from the truth may not change the arrival times much, but could severely alter the computation

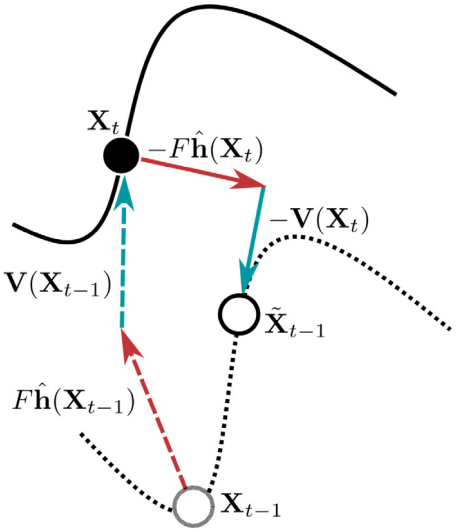

Fig. 3. Discrepancy over one time-step (not to scale) in the ODE backward tracing due to numerical inconsistency with the PDE forward reachability. In the ODE backward tracing (dashed), the external velocity (cyan arrow) and optimal heading direction (red arrow) are chosen to be explicit, i.e. those at point $\mathbf{X}_t$ (normal to the zero level set at this point), which leads the vehicle to $\tilde{\mathbf{X}}_{t-1}$. However, the PDE forward evolution (solid) was explicit; that is the external velocity and optimal heading values at $\mathbf{X}_{t-1}$ had been used in order to move from $\mathbf{X}_{t-1}$ to $\mathbf{X}_t$ (dashed cyan and red lines, respectively). For consistency, this should have been the path taken by the backward ODE, hence, the ODE should have been solved implicitly. If the inconsistency is kept, the computed position of the vehicle $\tilde{\mathbf{X}}_{t-1}$ differs from the numerically consistent position $\mathbf{X}_{t-1}$. With compounding, these errors may add up over time.

of the optimal path. Further, due to the entropy condition, $\boldsymbol{\phi}(\mathbf{x}, t)$ may be non-differentiable at the zero level set (Sethian, 1994). As is well known, finite difference and finite volume numerical schemes are diffusive of shocks and discontinuities, and these errors are amplified with time, mainly due to compounding of errors. For marine vehicles whose speed strongly depends on the heading or which can only travel in a few permissible directions, slight errors in the level set function computation can easily cause the computed heading direction to be vastly different from the optimal one. Hence, we employ high-order spatial and temporal schemes for the forward evolution of the level set function equation (17).

In our present case, for a simpler implementation of higher order schemes, the PDE is solved on a 3D structured grid, using the finite volume (FV) method. The optimal propulsion and advection terms are computed independently of each other. The boundary conditions do not have a direct impact on the growth of the reachability front, as it does not depend on the values of the level set function ($\boldsymbol{\phi}$) away from itself. To this end, we use radiation boundary conditions on $\boldsymbol{\phi}$ at all the boundaries.

We employ Essentially Non-Oscillatory (ENO) and Weighted Essentially Non-Oscillatory (WENO) schemes with up to 5th order accuracy (Shu and Osher, 1988; Jiang and Shu, 1996). The optimal propulsion term needs to be treated differently depending upon whether the vehicle exhibits isotropic motion or not. If the vehicle has isotropic speed, then the optimal propulsion term from Eq. (6) is solved using the Godunov scheme (Osher and Fedkiw, 2006). When the vehicle speed depends on its direction of travel, a maximization needs to be carried out. Appendix B presents the details of the numerical schemes as well as the maximization methods required for the optimal propulsion term. In conjunction with these spatial schemes, we utilize Total Variation Diminishing Runge–Kutta (TVD-RK) schemes of up to 3rd order accuracy for time marching (Osher and Fedkiw, 2006). The combination of ENO/WENO schemes with TVD-RK time marching ensures that the solution is Total Variation Bounded (TVB) (Osher and Fedkiw, 2006).

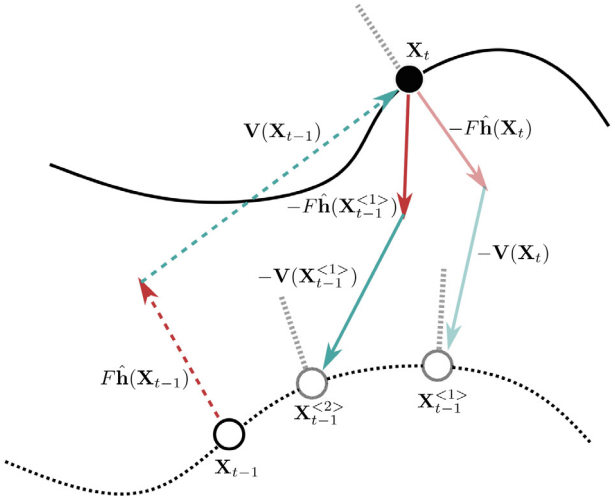

Fig. 4. Implicit backtracking scheme. A fixed-point iteration with the forward Euler backtracking scheme is schematized as an example. First, the optimal heading and the external velocity at point $\mathbf{X}_t$ and at time t (faint red and cyan arrows respectively) are used to reach the point $\mathbf{X}^{\langle 1\rangle}_{t-1}$. The normal to the zero level set at $\mathbf{X}^{\langle 1\rangle}_{t-1}$ at time $t-1$ is then computed (dotted gray line at $\mathbf{X}^{\langle 1\rangle}_{t-1}$), and this is used as the new optimal heading to move from $\mathbf{X}_t$ to $\mathbf{X}^{\langle 2\rangle}_{t-1}$. This process is repeated until the required convergence criterion is met.

4.4. Numerical schemes: Backward tracing

The optimal path is obtained by solving Eq. (7) backward in time, with $X(\mathbf{T}(\mathbf{x}_f : \mathbf{x}_s, 0)) = \mathbf{x}_f$. As all the time marching schemes that we utilize for Eq. (17) are explicit, *i.e.* explicit time integration is used, the consistent schemes for the optimal path computation must be implicit, which implies that iterative solvers are required, see Section 4.2. Further, the specifics of the scheme used for the characteristic computation must mimic the temporal scheme from the forward evolution computation.

Fig. 4 illustrates the underlying ideas behind the implicit backward tracing. For a fixed-point iteration, improved values are iteratively obtained by computing the predicted future position of the vehicle using the currently available heading and advective velocity values, and then using the values of these parameters from this position. To determine the optimal heading at any time, the normal direction to the local reachability front needs to be computed. This normal direction is then either directly used as the optimal heading direction, or is passed as an argument to the maximization described in Appendix B to obtain the optimal heading direction. The novel algorithm used for the computation of the normals in 3D is detailed in Appendix C. Appendix C also describes the implicit backward tracing schemes for time marching with forward Euler (TVD-RK 1), Heun's method (TVD-RK 2), and TVD-RK 3.

4.5. Numerical schemes: Vehicles with partially known motion

We now discuss numerical schemes for computing the optimal trajectory of vehicles with partially known motion, specifically due to the operator splitting approach used to solve Eqs. (15) and (16).

Forward evolution. As operator splitting is utilized to solve Eqs. (15), splitting errors are made. The order of the splitting error depends on the specifics of the splitting method utilized. Two popular operator splitting techniques are Lie splitting (MacNamara and Strang, 2016) and Strang splitting (Strang, 1968) which are at least 1st and 2nd order accurate respectively. Lie splitting simply involves explicitly solving Eq. (15a) followed by Eq. (15b) over one numerical time step each, and then adding the respective contributions. Strang splitting on the other hand involves solving Eq. (15a) over half a numerical time step and updating the field $\boldsymbol{\phi}(\mathbf{x}, t)$ with the outcome. Then Eq. (15b) is solved over one numerical time step using the updated field $\boldsymbol{\phi}(\mathbf{x}, t)$, and the results are updated. Finally, this new field is used to solve Eq. (15a) another half numerical time step to arrive at the final evolution. Under certain constraints on the external velocity and known component of the vehicle motion, these splitting methods can achieve higher orders of accuracy. For example, Lie splitting is 2nd order accurate whereas Strang splitting is exact for a vehicle following known motion along a fixed direction in a steady flow field. More numerical details including sufficient conditions for these splittings to yield tighter accuracy bounds can be found in Lanser and Verwer (1999) and Kulkarni and Lermusiaux (2019). In general, as long as the splitting error is of the same or higher order of accuracy as the numerical schemes employed for time marching, for resolved numerics, the accuracy of the complete numerical scheme is not affected by the splitting error.

Backward tracing. The implicit–explicit nature of the forward schemes along with the order of the operator splitting must be mimicked in backward tracing. The in-plane (in $\hat{\mathbf{n}}_\perp(t)$) motion can be computed by the backtracking algorithm in a consistent way to the forward time-marching used for the level set field. The trajectory point obtained (i.e. $\mathbf{X}^*_t$) is actually the projection of the exact point onto the $\hat{\mathbf{n}}_\perp(t)$ plane. The actual position is then computed by adding the displacement along $\hat{\mathbf{n}}(t)$ due to the vehicle velocity and the local flow velocity. This contribution can be either explicit or implicit, as shown by Eqs. (19) and (20),

$$\frac{\mathbf{X}^*_t - \mathbf{X}_{t+\Delta t}}{\Delta t} = F_\perp(\hat{\mathbf{h}}_\perp, \mathbf{X}_{t+\Delta t}, t+\Delta t)\,\hat{\mathbf{h}}_\perp(t+\Delta t) + \mathbf{V}_\perp(\mathbf{X}_{t+\Delta t}, t+\Delta t)\,,$$
$$\text{where}\quad \hat{\mathbf{h}}_\perp(t+\Delta t) = \arg\max_{\hat{\mathbf{h}}_\perp(\mathbf{X}_{t+\Delta t}, t+\Delta t)} \Big(F_\perp(\hat{\mathbf{h}}_\perp, \mathbf{X}_{t+\Delta t}, t+\Delta t) \tag{19}$$
$$\hat{\mathbf{h}}_\perp(\mathbf{X}_{t+\Delta t}, t+\Delta t)\cdot\nabla\boldsymbol{\phi}(\mathbf{X}_{t+\Delta t}, t+\Delta t)\Big)\,.$$

$$\frac{\mathbf{X}^{\langle k+1\rangle *}_t - \mathbf{X}_{t+\Delta t}}{\Delta t} = F_\perp(\hat{\mathbf{h}}_\perp, \mathbf{X}^{\langle k\rangle *}_t, t)\,\hat{\mathbf{h}}_\perp(t) + \mathbf{V}_\perp(\mathbf{X}^{\langle k\rangle *}_t, t)\,,$$
$$\text{where}\quad \hat{\mathbf{h}}_\perp(t) = \arg\max_{\hat{\mathbf{h}}_\perp(\mathbf{X}^{\langle k\rangle *}_t, t)} \Big(F_\perp(\hat{\mathbf{h}}_\perp, \mathbf{X}^{\langle k\rangle *}_t, t)\,\hat{\mathbf{h}}_\perp(\mathbf{X}^{\langle k\rangle *}_t, t)\cdot\nabla\boldsymbol{\phi}(\mathbf{X}^{\langle k\rangle *}_t, t)\Big)$$
$$\text{with}\quad \mathbf{X}^{\langle 0\rangle}_t = \mathbf{X}_{t+\Delta t}\,. \tag{20}$$

where $\mathbf{X}^*_t$ is the auxiliary position at time t when only the horizontal motion is accounted for. The effective velocity along $\hat{\mathbf{n}}(t)$ can be computed either explicitly (Eq. (21)) or implicitly (Eq. (22)),

$$\frac{\mathbf{X}_t - \mathbf{X}^*_t}{\Delta t} = -\left(V_z(\mathbf{X}^*_t, t) + F_n(\mathbf{X}^*_t, t)\,\hat{\mathbf{n}}(\mathbf{X}^*_t, t)\right)\,, \tag{21}$$

$$\frac{\mathbf{X}^{\langle k+1\rangle}_t - \mathbf{X}^*_t}{\Delta t} = -\left(V_z(\mathbf{X}^{\langle k\rangle}_t, t) + F_n(\mathbf{X}^{\langle k\rangle}_t, t)\,\hat{\mathbf{n}}(\mathbf{X}^{\langle k\rangle}_t, t)\right) \quad \text{with}\quad \mathbf{X}^{\langle 0\rangle}_t = \mathbf{X}^*_t\,. \tag{22}$$

4.6. Computational cost

We now look at the asymptotic computational complexity for the level set based time-optimal path planning in 3D environments. In all the considered examples, we numerically solve the forward evolution of the reachability front (either Eqs. (6) or (4)) using the finite volume method. The asymptotic computational complexity is a function of the grid size. In this analysis, we assume that there are approximately n grid points in each direction, and thus the total number of grid points in the domain (denoted by N) is about $N \approx \mathcal{O}(n^3)$.

Cost of solving the forward evolution of the reachable set in 3D. To solve the forward evolution of the reachability front, the level set equation is solved in the entire domain. The computational cost per time step for this is $\mathcal{O}(n^3)$ (Adalsteinsson and Sethian, 1995). The number of numerical time steps (K) that the solver runs for is directly related to the optimal travel time of the vehicle: $K = T(\mathbf{x} : \mathbf{x}_0, 0)/\Delta t$. As the optimal travel time of the vehicle is not known a priori, it is not possible to estimate the total number of time steps (K) to begin with.

Further, as we use explicit time marching to solve the level set PDE, the numerical time step Δt is inversely related to the number of grid points N, which makes K directly proportional to N. Instead of solving the PDE over the entire domain, one can use the narrow-band level set method (Adalsteinsson and Sethian, 1995) and solve the PDE only around the zero level set, reducing the computational cost from $\mathcal{O}\left(n^3\right)$ to $\mathcal{O}\left(dn^2\right) \approx \mathcal{O}\left(n^2\right)$, where $d\ (\ll n)$ is the bandwidth.

Cost of performing the maximization of the optimal propulsion term. If solving Eq. (4) with an analytical maximization is not possible, one can construct a look-up table prior to the forward evolution that contains the optimal heading direction for every direction of the outward normal (see Appendix B). This look-up table needs to only be constructed once, and its cost is directly proportional to the resolution used to discretize the optimal heading and outward normal directions. Specifically, if the optimal heading space is discretized in $\mathcal{O}\left(N_h^2\right)$ points (both the polar and the azimuthal directions contain $\mathcal{O}\left(N_h\right)$ points) and similarly the outward normal space is discretized in N_n^2 points, then the construction cost of the maximization look-up table is $\mathcal{O}\left(N_h^2 N_n^2\right)$.

Cost of solving the forward evolution of the reachable set for vehicles with partially known motion. For vehicles with partially known motion, the level set PDE only needs to be solved in 2 dimensions, and hence the computational cost per time step now becomes $\mathcal{O}(n^2)$ (Adalsteinsson and Sethian, 1995). Further, if analytical maximization is not possible, then the cost of constructing the look up table is $\mathcal{O}\left(N_h N_n\right)$, as the maximization is only performed in 2D (and not in 3D). Finally, the equation describing the vertical component of the reachable set growth is simply solved in 1D, and hence its cost is $\mathcal{O}(n)$. Thus the net cost of computing the forward evolution of the reachable set for vehicles with partially known motion is $\mathcal{O}\left(n^2+n\right)$ instead of $\mathcal{O}\left(n^3\right)$. Similarly to the 3D case, if the level set PDE is solved using the narrow-band level set method, the computational cost reduces to $\mathcal{O}(nd+n) \approx \mathcal{O}(n)$.

Cost of backward tracing of the optimal path. The backward tracing of the optimal path is simply done by solving an ODE, and hence the cost of this operation per time step is simply $\mathcal{O}(1)$, given the optimal heading direction is available. In order to obtain this optimal heading direction, one may need to construct the local outward normal to the reachability front and refer to the look-up table. However, these costs are assumed constant, and are much smaller than the forward evolution PDE solve costs.

Computational infrastructure used. All the analytical and realistic simulations presented in Sections 5 and 6 respectively were performed in MATLAB on a single quad-core Intel i7-4790 CPU clocked at 3.60 GHz. MATLAB's internal vectorization/parallelization for matrix–vector operations was enabled for all computations. The computational times required for the forward evolution of the reachable set and backward tracing of the optimal path for these applications are mentioned in their respective analyses.

5. Applications in benchmark three-dimensional analytically known flow fields

To verify schemes and benchmark accuracy, we now apply the exact time-optimal path planning in three 3D analytical flow fields. First, we study optimal path planning in a uniform advective flow. Analytical solution for the travel time are obtained, which allows quantifying errors in our algorithm. Second, a pulsating 3D vortical flow is used to benchmark the accuracy of our path planning in 3D dynamic flows with semi-analytical optimal trajectories and duration. Third, path planning in an analytical 3D double gyre–shear flow is studied. We effectively depict the ability to account for velocity fields that are spatially and temporally variable and also the ability to handle path planning for swarms of vehicles starting from the same location, where only a single forward PDE computation is required — this reduces the computational cost as compared to heuristic schemes with independent computations for each of the vehicles.

5.1. Validation in uniform velocity field

A theoretical value of the optimal travel time between a given pair of start and end points can be obtained for vehicles moving with isotropic speed in a uniform advective flow field. Let this advective flow be denoted as $\mathbf{V}(\mathbf{x},t) = \mathbf{V}_0 = (u_0, v_0, w_0)$ for all $\mathbf{x}$ and t.

To derive the optimal travel time, we consider the inertial reference frame moving with velocity $\mathbf{V}_{frame} = \mathbf{V}_0$. The advective velocity field is absent in this frame. However, the effective target position will now be $\mathbf{x}_f^* = \mathbf{x}_f - T \cdot \mathbf{V}_0$, if T is the sought optimal travel time. In the absence of any advective velocity field, the optimal path between $\mathbf{x}_s$ and $\mathbf{x}_f^*$ is a straight line joining these points, and the required travel time is given by $|\mathbf{x}_f^* - \mathbf{x}_s|/F$, which must be equal to T. We thus have

$$T = \frac{|\mathbf{x}_f^* - \mathbf{x}_s|}{F} = \frac{|\mathbf{x}_f - \mathbf{x}_s - T \cdot \mathbf{V}_0|}{F} . \tag{23}$$

Defining $\mathbf{x}_f - \mathbf{x}_s = \boldsymbol{\delta} = (\delta_x, \delta_y, \delta_z)$, Eq. (23) leads to a quadratic equation for T, with at most one non-negative root,

$$T = \frac{-\left(\boldsymbol{\delta} \cdot \mathbf{V}_0\right) + \sqrt{\left(\boldsymbol{\delta} \cdot \mathbf{V}_0\right)^2 + \left(F^2 - |\mathbf{V}_0|^2\right)|\boldsymbol{\delta}|^2}}{\left(F^2 - |\mathbf{V}_0|^2\right)} . \tag{24}$$

For $F = |\mathbf{V}_0|$, Eq. (24) fails to hold. However Eq. (23) then reduces to a linear equation, with:

$$T = \frac{|\boldsymbol{\delta}|^2}{2\boldsymbol{\delta} \cdot \mathbf{V}_0} . \tag{25}$$

For $F \geq |\mathbf{V}_0|$, T is always real. This implies that, in such cases all points in the domain can be reached in a finite time. This is a direct consequence of the fact that Eq. (6) can be reduced to a modified Eikonal equation when $F \geq |\mathbf{V}_0|$ (Lolla and Lermusiaux, 2020).

For the purposes of the simulation, we consider a unit domain. The start and the target positions are $\mathbf{x}_s = (0.25, 0.30, 0.40)$ and $\mathbf{x}_f = (0.70, 0.65, 0.80)$, with the vehicle traveling at a non-dimensional speed of 0.1 units. The external velocity field is given by: $\mathbf{V}_0 = (0.050, 0.075, 0.065)$. Hence, $|\mathbf{V}_0| = 0.11 > F$, and the PDE is not Eikonal. The theoretical optimal time, computed using Eq. (24) for this setup is 3.377. Our discretization for this benchmarking example consists of a $100 \times 100 \times 100$ grid and a time step of 5×10^{-3}. We use the finite volume method with the 5th order WENO scheme for spatial gradients and TVD RK3 scheme for time marching (see Appendix B). The computed optimal time is 3.375, which is only off from the true value by 0.059 %. This amount is extremely small, and due to small truncation errors (resolution in time and space) and common computational inaccuracies (round-off errors, etc.). The computational times required for the forward evolution and the backward tracing of the optimal path were 24 s and 1.03 s respectively.

For uniform advective velocities, the zero level set grows as a sphere with radius $r = F \cdot t$, and is also advected along the velocity direction. That is, the center of this sphere lies at $\mathbf{x}_c = t \cdot \mathbf{V}_0$. This is clearly seen from Fig. 5, where the zero level set evolves as a sphere, and moves along the direction of the velocity. It can be shown that the optimal path is a straight line joining $\mathbf{x}_s$ and $\mathbf{x}_f$, as is observed.

5.2. Validation in spherical vortical flow

We now consider a pulsating vortical flow to benchmark the accuracy of the optimal trajectory and travel time of our path planning. The flow field is a sinusoidally pulsating version of the velocity field generated from the stream function for the Rossby–Haurwitz benchmark problem for the shallow water wave equations (Williamson et al., 1992), as reported in Townsend et al. (2016). It is defined in spherical coordinates by Eq. (26), where r is the radial coordinate with unit vector $\hat{\mathbf{r}}$, $\lambda \in [-\pi, \pi]$ is the azimuthal angle with unit vector $\hat{\lambda}$, $\theta \in [0, \pi]$

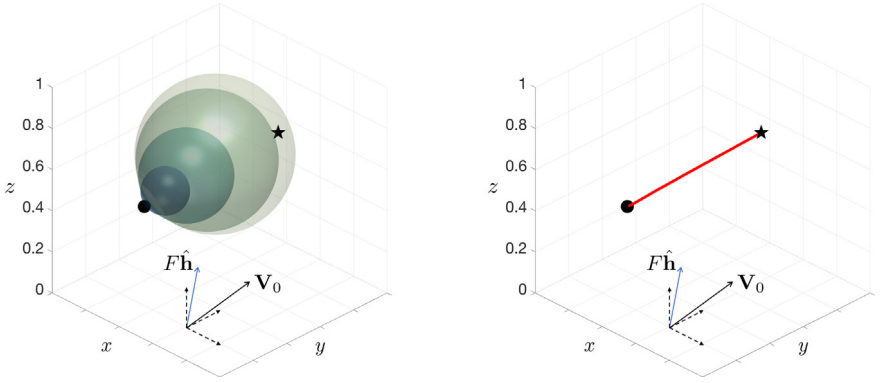

(a) Evolution of the zero level set (b) Optimal path

Fig. 5. Zero level set evolution and optimal path for a constant and uniform advective velocity field. The zero level sets at multiple intermediate times are plotted. The start position is represented by a black circle and the target position by a black star. The optimal path between the start and end positions, shown in red, is the straight line joining these two points. The external velocity field $\mathbf{V}_0$ and the vehicle velocity $F\hat{\mathbf{h}}$ are displayed by black and blue vectors, respectively.

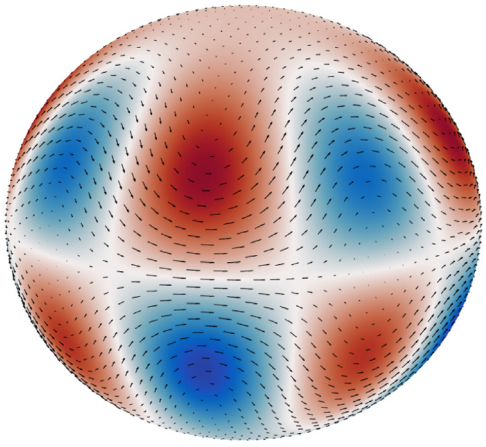

Fig. 6. The spherical vortical velocity field defined by Eq. (26) at $t = 0$ on a sphere of radius $r = 1$. Velocity vectors indicating the magnitude and direction of the velocity are overlaid on the vorticity field. This velocity field is generated from a stream function for the Rossby–Haurwitz benchmark problem for the shallow water wave equations (Williamson et al., 1992; Townsend et al., 2016), and has no radial component.

is the polar angle with unit vector $\hat{\boldsymbol{\theta}}$, and ∇_s is the gradient in spherical coordinates,

$$\mathbf{V}(r,\lambda,\theta,t) = \hat{\mathbf{r}} \times \nabla_s \boldsymbol{\psi}(r,\lambda,\theta,t)\,,$$
$$\text{where } \boldsymbol{\psi}(r,\lambda,\theta,t) = \cos\left(\frac{2\pi t}{\tilde{T}}\right)\left[\cos(\theta) + \sin^4(\theta)\cos(\theta)\cos(4\lambda)\right]. \tag{26}$$

Fig. 6 shows this flow field plotted at $t = 0$ on a sphere of $r = 1$. The velocity field is $\mathbf{V}(r,\lambda,\theta,t) = V_\lambda(r,\lambda,\theta,t)\hat{\boldsymbol{\lambda}} + V_\theta(r,\lambda,\theta,t)\hat{\boldsymbol{\theta}}$. The flow field has no component in the radial direction, and all the radial motions of the vehicle are thus due to its own propulsion. We utilize this fact to design a suitable test case to benchmark our 3D method. Specifically, we choose the destination of the vehicle for a given start location and travel time such that the analytical vehicle propulsion is always radially outwards.

Let us assume that the vehicle starts at location $\mathbf{x}_s = (r_s, \lambda_s, \theta_s)$ and requires a to-be-determined travel time of $\tilde{T}$ (fixed) to reach a given destination $\mathbf{x}_f = (r_f, \lambda_f, \theta_f)$. We assume that the vehicle can move isotropically and with a maximum speed F. The to-be-optimized velocity of the vehicle relative to the flow field is: $F(t)\hat{\mathbf{h}}(t) = F_r(t)\hat{\mathbf{r}} + F_\lambda(t)\hat{\boldsymbol{\lambda}} + F_\theta(t)\hat{\boldsymbol{\theta}}$ with $F_r(t)^2 + F_\lambda(t)^2 + F_\theta(t)^2 \le F^2$. The trajectory ODE of such a vehicle is thus:

$$\frac{d\mathbf{X}(t)}{dt} = F_r(t)\hat{\mathbf{r}} + \left(F_\lambda(t) + V_\lambda(r,\lambda,\theta,t)\right)\hat{\boldsymbol{\lambda}} + \left(F_\theta(t) + V_\theta(r,\lambda,\theta,t)\right)\hat{\boldsymbol{\theta}}\,. \tag{27}$$

Separating the components of Eq. (27), we have $\dot{r} = F_r(t)$, $r\sin(\theta)\dot{\lambda} = F_\lambda(t) + V_\lambda(r,\lambda,\theta,t)$, and $r\dot{\theta} = F_\theta(t) + V_\theta(r,\lambda,\theta,t)$. Upon integrating the radial component, we obtain:

$$\int_{r_s}^{r_f} dr = \int_0^{\tilde{T}} F_r(t)dt \le \int_0^{\tilde{T}} F dt\,,$$
$$\implies r_f = r_s + F_r(t)\tilde{T} \le r_s + F\tilde{T}\,. \tag{28}$$

From Eq. (28), we can set $r_f = r_s + F\tilde{T}$ (λ_f, θ_f still to be selected), which implies that the optimal vehicle will have to move radially outwards with speed F at all times, as any other choice will yield a larger travel time. As $F_r(t) = F$, this implies $F_\lambda(t) = F_\theta(t) = 0$. The other two components of the trajectory Eq. (27), the coordinates λ_f and θ_f, are thus defined by:

$$\dot{\lambda} = \frac{V_\lambda(r,\lambda,\theta,t)}{r\sin(\theta)} = \frac{V_\lambda(r_s + Ft,\lambda,\theta,t)}{(r_s + Ft)\sin(\theta)}\,,$$
$$\dot{\theta} = \frac{V_\theta(r,\lambda,\theta,t)}{r} = \frac{V_\theta(r_s + Ft,\lambda,\theta,t)}{r_s + Ft}\,. \tag{29}$$

As designed, the optimal travel time between the chosen start point $\mathbf{x}_s$ and the destination $\mathbf{x}_f$ is $\tilde{T}$. The vehicle always travels radially outwards with the maximum allowable speed F. The optimal trajectory $\mathbf{x}(t) = (r(t), \lambda(t), \theta(t))\ \forall\ t \in [0, \tilde{T}]$ can thus be semi-analytically computed using Eq. (29) in

$$\int_{\mathbf{x}_s}^{\mathbf{x}(t)} \begin{bmatrix} dr \\ d\lambda \\ d\theta \end{bmatrix} = \int_0^{\tilde{T}} \begin{bmatrix} F \\ V_\lambda/r\sin(\theta) \\ V_\theta/r \end{bmatrix} dt\,. \tag{30}$$

This completes our benchmark problem definition. To be specific, we choose the start location to be $\mathbf{x}_s = \left(0.1, 0, \frac{\pi}{4}\right)$, the travel time $\tilde{T} = 0.9$, and the vehicle speed $F = 1$. This implies that the exact destination $\mathbf{x}_f$ has the radial coordinate $r_f = 1.0$. Integrating Eq. (30), its azimuthal and polar coordinates are found to be $\lambda_f = -0.9754\pi$ and $\theta_f = 0.2277\pi$.

To evaluate our numerical integration of the forward level-set PDE (6) and backward ODE (7), we now compare the computed optimal travel time with its theoretical value $\tilde{T}$ and the computed optimal trajectory with its exact optimal trajectory, obtained by the semi-analytical integration of Eq. (30). The 3D path planning problem to be solved using the level set methodology is thus to predict the optimal trajectory for a vehicle with maximum speed $F = 1$ that is traveling from $\mathbf{x}_s = \left(0.1, 0, \frac{\pi}{4}\right)$ to $\mathbf{x}_f = (1.0, -0.9754\pi, 0.2277\pi)$ under the external dynamic velocity field $\mathbf{V}(r,\lambda,\theta,t)$ given by Eq. (26). We solve this problem on a domain $\Omega = [-2,2] \times [-2,2] \times [-2,2]$, using the finite volume method with 200 grid points in each direction, and a numerical time step of $\Delta t = 0.001$. A 5th order WENO scheme is used for spatial

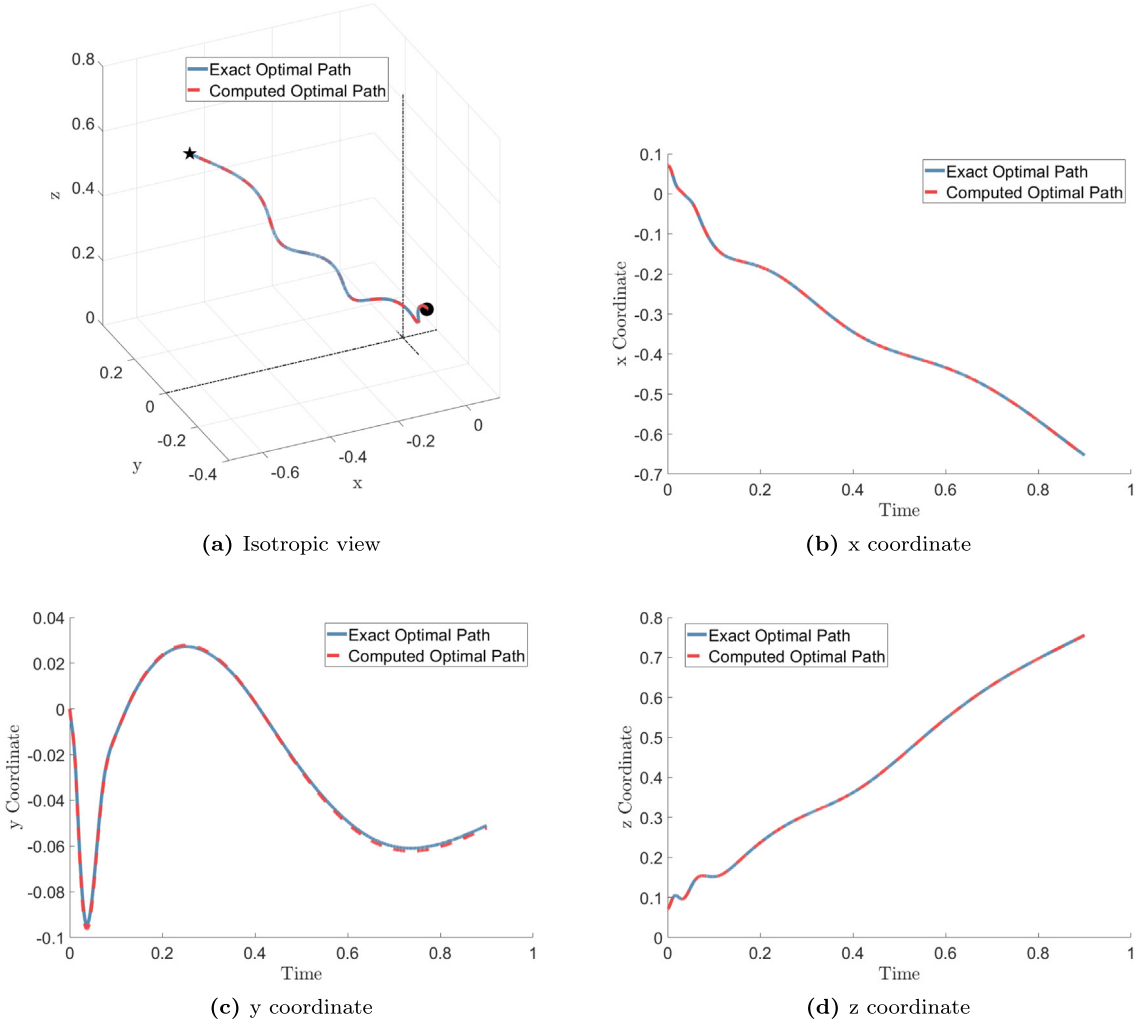

(a) Isotropic view (b) x coordinate

(c) y coordinate (d) z coordinate

Fig. 7. Semi-analytical exact (solid) and numerically predicted (dashed) time-optimal paths for a vehicle traveling from $\mathbf{x}_s = \left(0.1, 0, \frac{\pi}{4}\right)$ to $\mathbf{x}_f = (1.0, -0.9754\pi, 0.2277\pi)$ with speed $F = 1$. The computed optimal path is obtained by numerical integration of the forward Hamilton–Jacobi level set PDE up to $\mathbf{x}_f$ followed by backward tracing the trajectory ODE starting from $\mathbf{x}_f$. The semi-analytical optimal path is obtained by integrating Eq. (30) from $t = 0$ to $t = \tilde{T}$.

gradients and a TVD RK3 scheme for time marching (see Appendix B). As the external velocity field has no radial component, the reachability front grows as a sphere with its rate of radius increase being $F = 1$ (not shown). The computational time required is found to be 341.09 s for this forward evolution of the reachability front and 1.34 s for backtracking the time-optimal path.

The optimal time required for traveling from $\mathbf{x}_s$ to $\mathbf{x}_f$ is predicted to be $T = 0.902$, which is extremely close to the exact value of $\tilde{T} = 0.9$, with a relative error of 0.22%. Fig. 7 compares the semi-analytical trajectory (integrating Eq. (30) using the forward Euler method and a time step of $\Delta t = 0.001$) to the level-set computed backtracked trajectory in 3D and their components along the X, Y, and Z axes. We find that the computed trajectory is also extremely close to the semi-analytical trajectory at all times, in all the coordinates.

5.3. Application in three-dimensional analytical double Gyre–Shear flow

We now verify schemes with the analytical double gyre flow, that is a periodic, unsteady, and divergence-free velocity field (Shadden et al., 2005; Froyland and Padberg, 2009). Note that, this model is not a real fluid flow, in that it is not obtained as a solution to the Navier–Stokes' PDEs, but is a simplification of the double gyre pattern that frequently occurs in geophysical flows (Coulliette and Wiggins, 2001; Lolla et al., 2014b; Subramani and Lermusiaux, 2016). We consider this flow in the domain $(0, 2) \times (0, 1) \times (0, 1)$. The classic double gyre is a two-dimensional flow in space whose non-dimensional velocity field is analytically described by

$$v_x = -\pi A \sin(\pi f(x)) \cos(\pi y) \qquad v_y = \pi A \cos(\pi f(x)) \sin(\pi y) \frac{df}{dx}, \tag{31}$$

where,

$$f(x) = a(t)x^2 + b(t)x \tag{32}$$

$$a(t) = \epsilon \sin(\omega t) \tag{33}$$

$$b(t) = 1 - 2\epsilon \sin(\omega t)\,. \tag{34}$$

To create a 3D flow field from Eq. (31), we add an unsteady parabolic velocity profile for the Z direction that bears positive values in the region of the first gyre and negative values within the other gyre. Specifically, the Z velocity is given by:

$$v_z = xy(2 - x)(1 - y)\,(1 + \epsilon \sin(\omega t) - x)\,. \tag{35}$$

The velocity field is depicted in Fig. 8. The parameters used are: $A = 0.1$, $\epsilon = 0.1$, $\omega = \pi/5$. The vehicle speed is set to 0.05 and a $200 \times 100 \times 100$ grid with a time step of 5×10^{-3} is used in a finite volume setup with the 5th order WENO scheme for spatial gradients and TVD RK3 scheme for time marching (see Appendix B).

This example demonstrates a one-to-all broadcast, where multiple vehicles leave from the same start point in order to travel to different

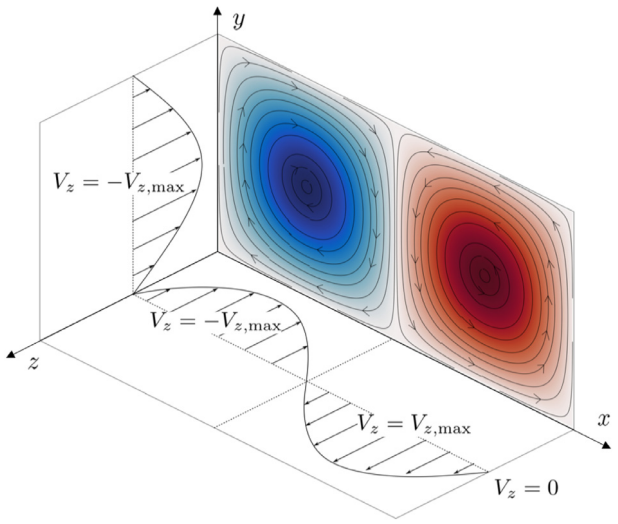

Fig. 8. Three-dimensional analytical double gyre–shear flow velocity field. The classic analytical double gyre flow exists in the X–Y plane, and its streamlines are overlaid on a vorticity plot for the same flow field. The Z direction has a double-parabolic velocity profile, whose projection is shown over the X–Z and the Y–Z planes.

target locations. With our PDE approach, such a broadcast only requires one level set evolution per start point, and hence it is computationally advantageous. The zero level set is evolved from the start point until all the destination positions lie on or inside it. The time at which the reachability front crosses a particular destination position is noted, and the optimal path is backtracked from this stored time until the start time. Hence, increasing the number of target positions only increases the cost of the backtracking ODE computation, which is much less than that of the forward evolution PDE. Specifically, the forward evolution of the reachability front required 82.33 s, whereas the backward tracing of the three optimal paths required 0.87 s (green), 1.41 s (orange) and 1.56 s (red), respectively.

Fig. 9 shows the predicted optimal paths to be followed by the vehicles to reach the respective destinations in shortest time. It is clear that the vehicles utilize the background flow field to their advantage. Even though they travel much longer distances (as compared to straight line paths), they do so at a higher effective speed, thus reaching in shortest time.

6. Applications in three-dimensional realistic oceanic flow fields

This section integrates realistic ocean modeling and time-optimal path prediction for common types of marine vehicles. Operations are planned for the complex four-dimensional (time–space) ocean flow fields of the Middle Atlantic Bight region. Three types of marine vehicles are considered: (i) vehicles with isotropic propulsion, (ii) vehicles with anisotropic speeds, specifically oceanic floats that can propel vertically by adjusting buoyancy, but are advected in the horizontal (Rudnick et al., 2004), and (iii) typical marine gliders that perform a vertical sinusoidal (yo-yo) motion, which reduces the path planning problem to a two-dimensional one as shown in Section 3. We first describe the 3D regional dynamics, our data-assimilative multi-resolution ocean modeling, and our computational time-optimal path planning setup. We then describe the evolution of the reachability front for these vehicles, highlighting how the underlying dynamic flow features affect this evolution. Finally, we analyze the actual time-optimal paths and show how each type of optimal vehicle intelligently utilizes the currents most beneficial and avoids the most adverse, in accord with its type.

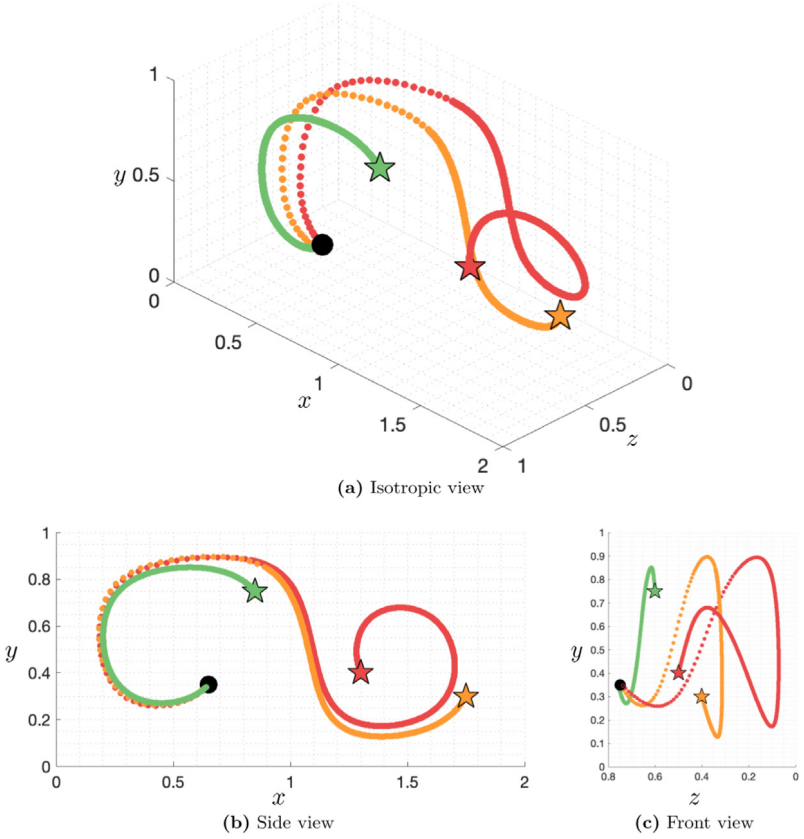

Fig. 9. Predicted time-optimal paths for vehicles traveling to different target locations in a 3D double gyre–shear flow. The dotted sections of the path represent the part of the trajectory where the external flow field is in the negative Z direction.

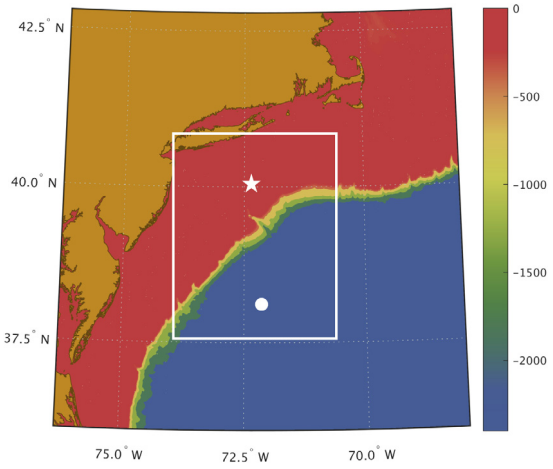

Fig. 10. Open domain (white rectangle) for realistic path planning missions in the Middle Atlantic Bight region, overlaid on bathymetry. The circle is the start position and the star is the target position of the mission, just north of the Hudson Canyon.

6.1. Ocean modeling and oceanography

The Middle Atlantic Bight region, off the coast of New Jersey, offers a variety of flow features interacting on multiple scales (Linder and Gawarkiewicz, 1998; Lozier and Gawarkiewicz, 2001; Lentz, 2008; Wilkin et al., 2018; Kelly and Lermusiaux, 2016). They include the Gulf Stream, shelf-break front, coastal jets, tidal currents, internal tides, and also Hudson river outflow. Such conditions provide challenging environments for autonomous missions. Fig. 10 shows the simulation domain overlaid on bathymetry, from $37.56°N$ to $40.99°N$, and $73.97°W$ to $70.54°W$. The white circle and the star denote the start $(37.90°N, 72.22°W)$ and target positions $(39.85°N, 72.30°W)$ for our planning missions, respectively (both positions at the surface).

The multi-scale ocean dynamics in this region is simulated using the MIT Multidisciplinary Simulation Estimation and Assimilation System (MSEAS) (Haley Jr. and Lermusiaux, 2010; Haley Jr. et al., 2015). MSEAS is used for fundamental research as well as realistic applications such as monitoring (Lermusiaux et al., 2007), real-time ecosystem and acoustic predictions (Beşiktepe et al., 2003; Xu et al., 2008; Lermusiaux et al., 2011), and environmental management (Cossarini et al., 2009).

The specific currents used for path planning are from a data-assimilative MSEAS re-analysis for August 28, 2006 up to September 9, 2006 (Haley Jr. et al., 2015; Subramani et al., 2017a). The data were collected as a part of the Shallow Water '06 (SW06) initiative (WHOI, 2006; Lermusiaux et al., 2006a; Newhall et al., 2007; Tang et al., 2007; Chapman and Lynch, 2010; Lin et al., 2010). MSEAS solves the nonlinear free-surface hydrostatic primitive-equation (PE), configured with generalized-level vertical-coordinates and implicit two-way nested computational domains (Haley Jr. and Lermusiaux, 2010). In the horizontal, the domains have a

3 km and 1 km grid resolution, respectively, and in the vertical, they each employ 100 levels optimized to the thermocline and flow structures. The tidal-to-mesoscale ocean re-analysis is initialized with objectively-analyzed temperature, salinity, and velocity fields for Aug 14, 2006. Two multiscale-in-space analyses (Lermusiaux, 1999, 2002), inshore and offshore of the expected shelfbreak front, are combined using a shelfbreak-front feature model (Lermusiaux, 1999; Gangopadhyay et al., 2003). The Gulf Stream is initialized using synoptic and historical CTD profiles as well as estimates of its position based on SST and NAVOCEANO feature analyses. High-resolution barotropic tides (Logutov and Lermusiaux, 2008) based on the TPXO7.2 surface-tide velocities and elevation (Egbert and Erofeeva, 2002) for Aug 14 2006 are merged with the subtidal initial fields, following Haley Jr. et al. (2015). The re-analysis free-surface PE simulation is then integrated for 42 days. During integration, the ocean data collected during the AWACS and SW06 exercises (Tang et al., 2007) as well as data of opportunity (NMFS, etc.) are assimilated. Finally, the numerical and sub-grid-scale parameters are tuned for the region by comparison of many PE simulations with independent in situ SW06 measurements.

6.1.1. Ocean flows and regional dynamics

In the present period, we observe that the optimal paths for the AUV (with isotropic speed) and the float go down to a maximum depth of 22 m (the float travels deeper, but for an extremely short duration), and hence we focus on the top 20 m of the ocean flows over the considered time of interest. Figs. 11, 12, and 13 plot the daily averaged horizontal currents at 0 m, 10 m, and 20 m depth, respectively. Also shown are the daily position of the (isotropic) AUV — pink circle denotes the current position (*i.e.* position on the considered day at 00 UTC) whereas the gray circle(s) denote the horizontal position(s) of the vehicle on the past day(s). Note that this is simply the horizontal location of the vehicle (*i.e.* discarding depth); the vehicle may not be at the particular depth at the considered instant. We also plot the daily averaged horizontal currents, depth averaged over the first 90 m in Fig. 14. This is effectively the flow field experienced by the glider performing sinusoidal (yo-yo) motion. The daily position of the glider and its history are denoted in pink and gray, similar to the previous figures.

The Gulf Stream is clearly seen in the southeast corner of the domain at all depths as well as the depth averaged fields, with velocities reaching 2 m/s. The meandering shelfbreak front jet, flowing to the west-southwest and close to the 100 m isobath is also visible (Lermusiaux, 1999; Linder and Gawarkiewicz, 1998), especially in Fig. 14. On August 28 (Figs. 11(a), 12(a), 13(a), 14(a)), there is a northeast-to-southwest jet just north of the Gulf Stream with speeds up to 25 cm/s. This flow is almost non-existent at the surface, but gets stronger with depth. There is also a local northward flow (between the Gulf Stream and the said jet) locally at the mission start point. On the shelf, the surface flow reverses due to southwestward winds on August 29, developing first along the coast of Long Island and intensifying to a midshelf westward-southwestward flow by August 30, as especially seen in the depth-averaged velocities (Fig. 14(b), (c)) and at the surface (Fig. 11(b), (c)). We also find that the said northeast–southwest jet strengthens at the surface and a bit deeper during this period, and a cyclonic eddy feature develops north of the Gulf Stream (near $38.9°N$, $71.9°W$), at depths of 10 m onwards (Figs. 12(b), (c), 13(b), (c)), with its northern side linked to the south-southwest shelfbreak front jet. Our vehicles take advantage of this eddy, as will be shown in Section 6.4.

Tropical storm Ernesto passes over the domain during September 1–3. The operational region mostly sees the northeastern edge of the storm as it proceeds northward. The ocean response is a northwestward flow at the surface, 2–3 times stronger than on August 30 and shelf wide with intensification near the coast (Fig. 11(e)–(g)). Due to 3D downwelling, the flow changes direction with depth: it is reversed to the south-southwest at 20 m (Figs. 13(e)–(g), 14(e)–(g)). After the storm, the main flow on the shelf south of New Jersey is generally southwestward, parallel to the coast and shelfbreak. It reaches a barotropic magnitude of 5–10 cm/s, with currents decaying with depth. This midshelf flow is a remnant of the shelf response to Ernesto, partly supported by a local cross-shelf density gradient (not shown) that Ernesto established. On September 6, the shelfbreak front jet reaches a barotropic strength of 10–20 cm/s (Fig. 11(j)), in part due to the minor wind event between 00 to 17 UTC on that day. Finally, weak density-driven eddies and currents occur on the shelf during the whole period and affect the optimal paths.

6.2. Computational setup and simulation details

Our first example models AUVs that can more or less propel in any direction at their operating speed. We assume here that the vehicle has

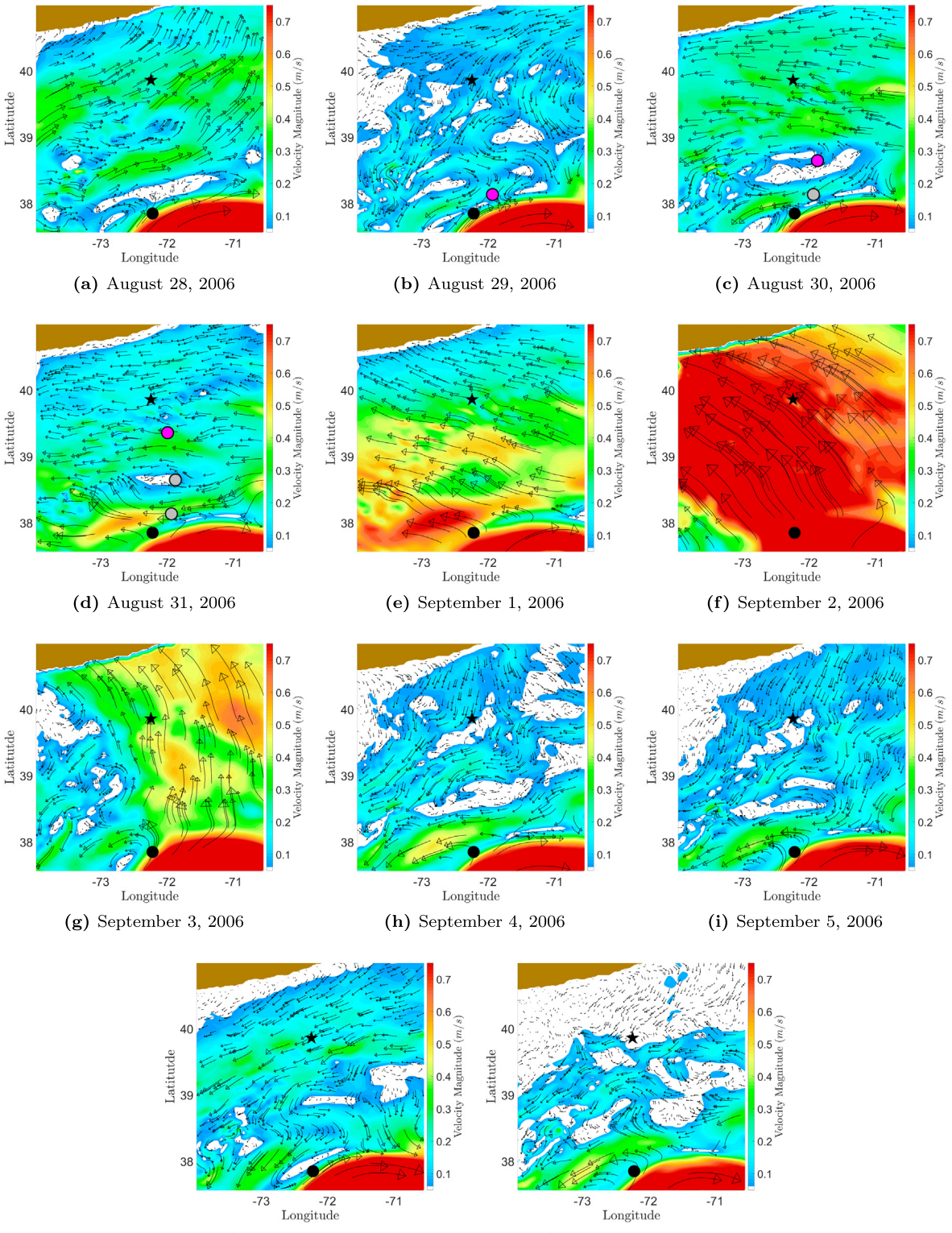

(a) August 28, 2006 (b) August 29, 2006 (c) August 30, 2006

(d) August 31, 2006 (e) September 1, 2006 (f) September 2, 2006

(g) September 3, 2006 (h) September 4, 2006 (i) September 5, 2006

(j) September 6, 2006 (k) September 7, 2006

Fig. 11. Daily ocean flow field at the surface (0 m depth) in the Middle Atlantic Bight shelfbreak front region, as re-analyzed by MSEAS. Flow patterns are illustrated by their vectors, overlaid on flow magnitude (colored in m/s). The pink circles highlight the position of the isotropic AUV on the considered date (at 00 UTC), and the gray circles show its locations from the past days (also at 00 UTC).

a maximum propulsion speed of 50 cm/s and a maximum allowable depth of 100 m, which is well within the typical range of such vehicles (Rudnick et al., 2004; Haley Jr. et al., 2009; Ramp et al., 2009). The second example looks at path planning for vehicles with heading-dependent propulsion speeds and constrained motion (Section 3.1). Particularly, we consider a vehicle that can propel only in the vertical; its motion in the horizontal plane is then only through flow advection. Most oceanic floats are able to maneuver this way, wherein their vertical propulsion is a result of changing their effective buoyancy (Gould et al., 2004). We assume that the float can travel at 10 cm/s vertically

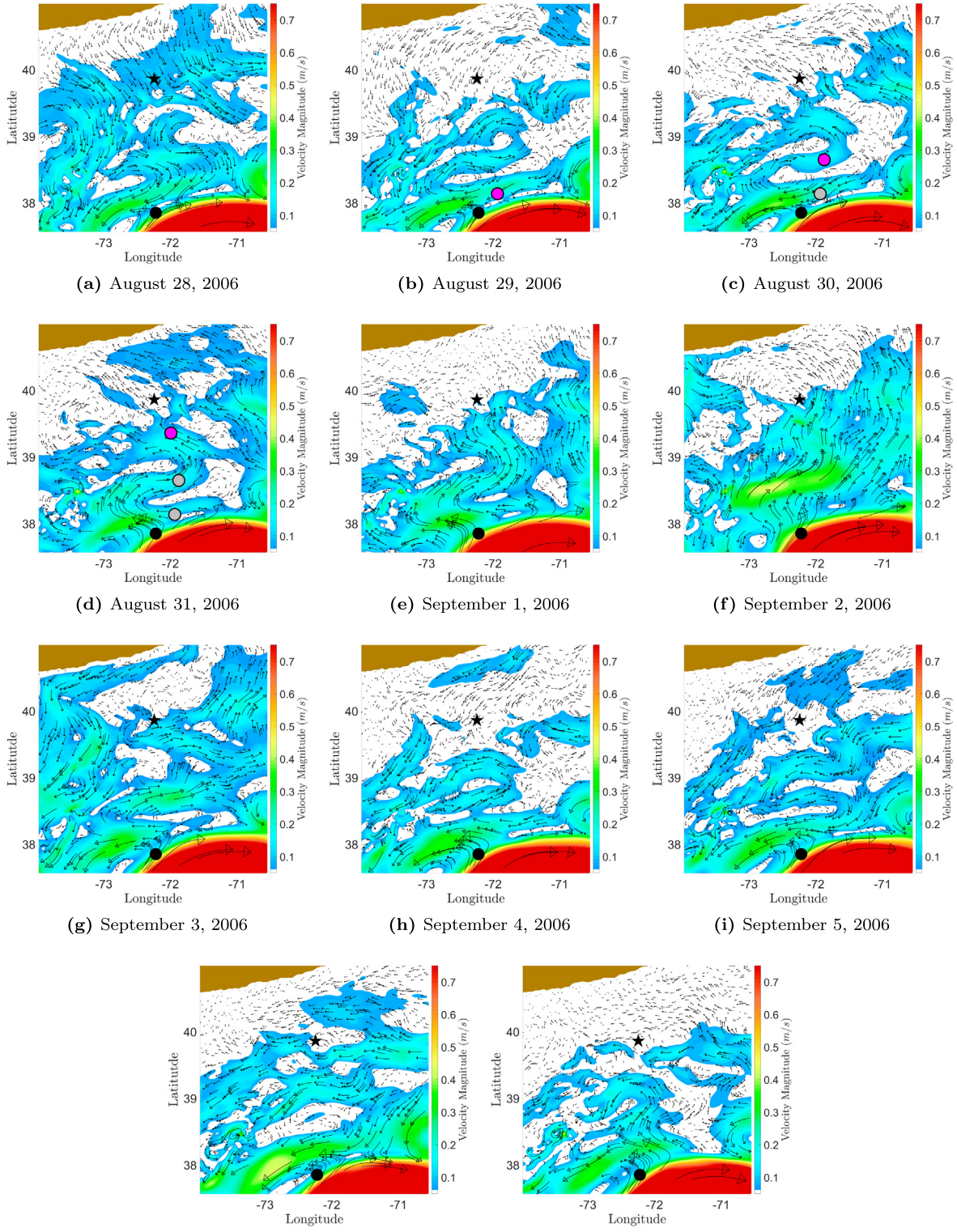

(a) August 28, 2006 (b) August 29, 2006 (c) August 30, 2006

(d) August 31, 2006 (e) September 1, 2006 (f) September 2, 2006

(g) September 3, 2006 (h) September 4, 2006 (i) September 5, 2006

(j) September 6, 2006 (k) September 7, 2006

Fig. 12. Daily ocean flow field at 10 m depth in the Middle Atlantic Bight shelfbreak front region, as re-analyzed by MSEAS. Flow patterns are illustrated by their vectors, overlaid on flow magnitude (colored in m/s). The pink circles highlight the position of the isotropic AUV on the considered date (at 00 UTC), and the gray circles show its locations from the past days (also at 00 UTC).

(but with no propulsion in the horizontal directions) and is allowed to travel at a maximum depth of 100 m. We finally showcase an underwater glider that performs a sinusoidal yo-yo motion, as typical for ocean data collection (Fan and Woolsey, 2014; Ramp et al., 2009; Haley Jr. et al., 2009; Leonard et al., 2010). In our example, we assume typical operational parameters to be similar to a Seaglider (Rudnick et al., 2004). The glider is assumed to slowly dive up to 90 meters in depth, with subsequent up-and-down motions with a period of 4 h. The average vertical speed is 1.25 cm/s. In the horizontal plane, the speed is assumed to be 50 cm/s (Stokey et al., 2005).

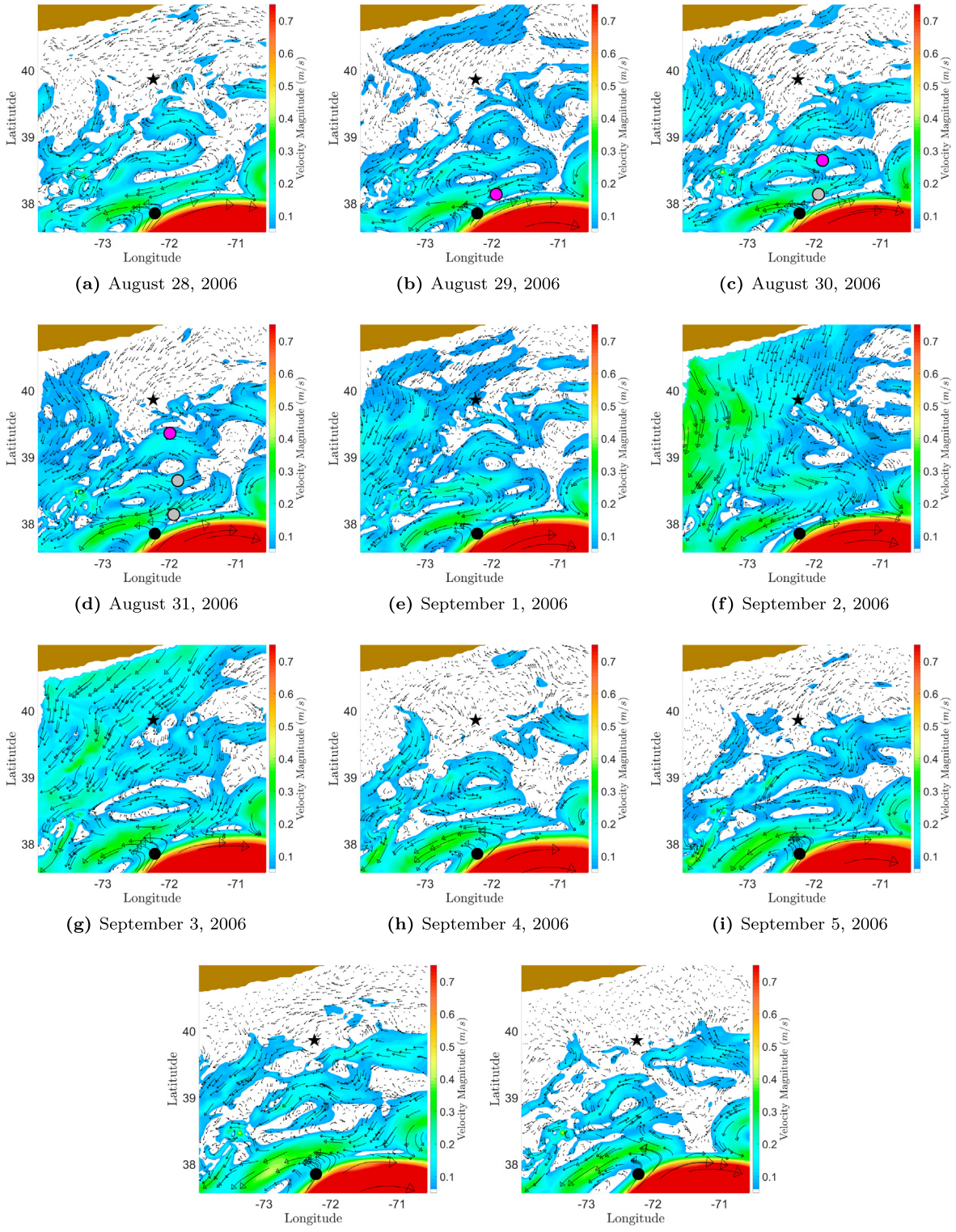

(a) August 28, 2006 (b) August 29, 2006 (c) August 30, 2006

(d) August 31, 2006 (e) September 1, 2006 (f) September 2, 2006

(g) September 3, 2006 (h) September 4, 2006 (i) September 5, 2006

(j) September 6, 2006 (k) September 7, 2006

Fig. 13. Daily ocean flow field at 20 m depth in the Middle Atlantic Bight shelfbreak front region, as re-analyzed by MSEAS. Flow patterns are illustrated by their vectors, overlaid on flow magnitude (colored in m/s). The pink circles highlight the position of the isotropic AUV on the considered date (at 00 UTC), and the gray circles show its locations from the past days (also at 00 UTC).

Our 3D path planning numerically solves the exact non-dimensional form of the forward Hamilton–Jacobi level set Eq. (18). We employ the finite volume method on a grid of 128 × 128 × 50 elements in the longitudinal, latitudinal, and vertical directions, respectively, where each grid cell has an approximate size of 2.32 km × 2.98 km × 2 m. A time step of 6 min (360 s) is used. We use the 5th order WENO scheme for the spatial terms and the TVD RK3 for time marching. In the case of partially known vehicle motion, the 3D path planning problem reduces to a 2D one (Section 3.2). Hence, simulations are carried out on a 2D grid of resolution 128 × 128 elements, with the rest

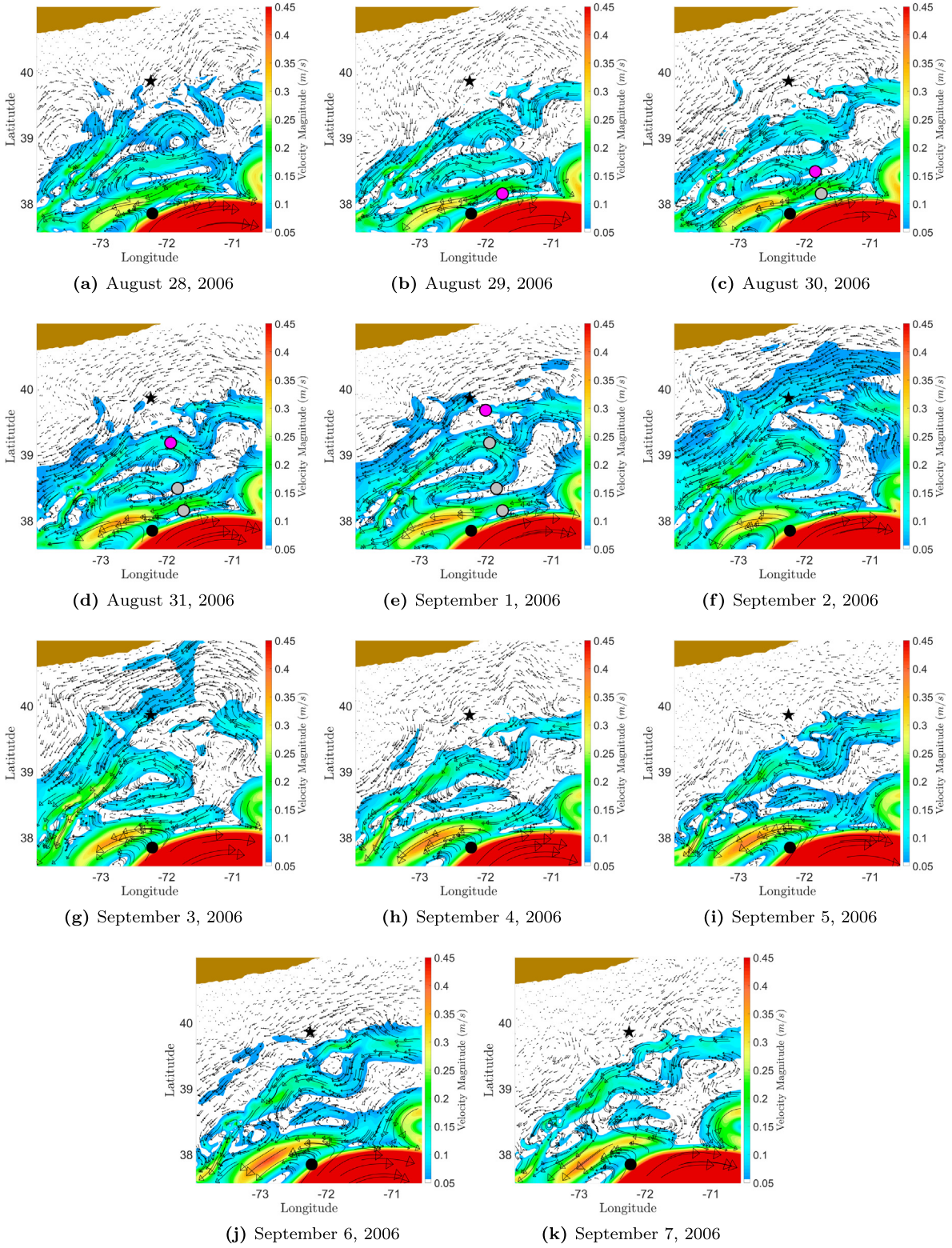

(a) August 28, 2006 (b) August 29, 2006 (c) August 30, 2006

(d) August 31, 2006 (e) September 1, 2006 (f) September 2, 2006

(g) September 3, 2006 (h) September 4, 2006 (i) September 5, 2006

(j) September 6, 2006 (k) September 7, 2006

Fig. 14. Daily ocean flow field averaged over the top 90 m in the Middle Atlantic Bight shelfbreak front region, as re-analyzed by MSEAS. Flow patterns are illustrated by their vectors, overlaid on flow magnitude (colored in m/s). The pink circles highlight the position of the glider (performing a sinusoidal yo-yo motion) on the considered date (at 00 UTC), and the gray circles show its locations from the past days (also at 00 UTC).

of the computational setup being as above. All the vehicles start their journey on August 28 at 00 UTC, from the same start location as stated above (ref. Fig. 10). The reachability front defined as the zero level set of ϕ is constructed by linear interpolation between grid points. Once the forward evolution of the reachability front is complete, backward tracing of the optimal trajectory is computed using the fully implicit backward tracing schemes obtained in Section 4 and further detailed in Appendix C. To compute this backtracked optimal path, we need

Table 2
Operating characteristics and summary of results for time-optimal path planning in the Middle Atlantic Bight region.

Vehicle type	Propulsion details	Optimal duration	Reachability front evolution	Optimal path
Isotropic AUV	50 cm/s in any direction	3.84 days	Fig. 15	Fig. 17
Float	No propulsion in the horizontal plane; 10 cm/s in the vertical	9.53 days	Fig. 16	Fig. 18
Glider	50 cm/s in the horizontal plane; sinusoidal dives (with a 4 h period) in the vertical	4.15 days		Fig. 19

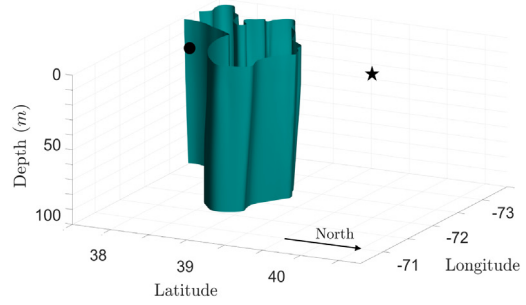

(a) Reachability front on Aug. 29, 00:00:00 UTC (1 day)

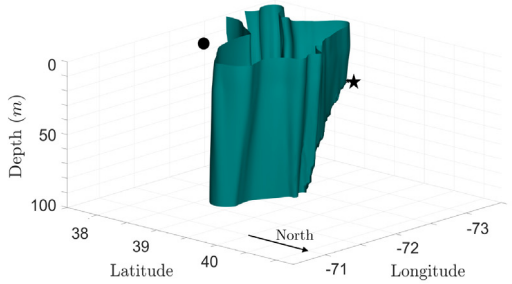

(b) Reachability front on Aug. 30, 00:00:00 UTC (2 days)

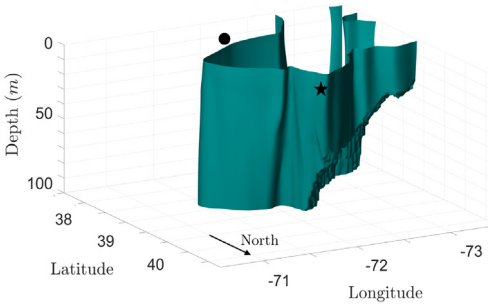

(c) Reachability front on Aug. 31, 00:00:00 UTC (3 days)

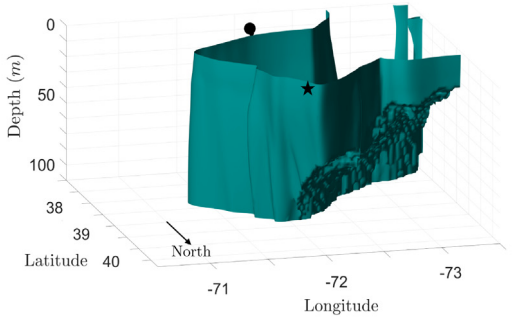

(d) Reachability front on Sep. 1, 20:17:22 UTC (3.84 days)

Fig. 15. Evolution of the zero level set (not to scale) in the Middle Atlantic Bight region for a vehicle with isotropic speed. The level set evolves as curtains due to the weak depth-variability of the dominant horizontal velocity field. Further, the level set growth is halted whenever it is near the sea-floor. This leads to the jagged surfaces in sub-figures (c) and (d). The level set evolution is shown from different viewpoints so as to better understand the global picture.

to compute the normal direction to the reachability front at certain locations. Appendix C describes the algorithm used to compute such normal directions at arbitrary locations on the reachability front.

Table 2 summarizes the considered operating characteristics, the optimal travel time results, and the relevant figure numbers that contain the reachability front evolutions and optimal paths.

6.3. Evolution of the reachable sets

Isotropic AUV. Fig. 15 plots the growth of the zero level set (the reachability front) for the AUV with isotropic propulsion. We observe that the zero level set quickly reaches the deepest limit of the simulation domain, and then evolves as a deforming and sloping curtain, with clearly visible creases. These variations of the curtain along the vertical happen due to the following reasons. First, the flow in this region is mainly dominated by surface tides, wind-driven flows, and thermocline intensified currents and eddies. This means that the variability of the horizontal velocities along the vertical direction is much smaller than the velocities themselves. Most horizontal motions have small and local reversals in the first 100 m depth; there are only a few regions and times where a flow reversal with depth is observed. These phenomena prompt the zero level set to grow as curtains. Second, the small variations and shifts of the zero level set with depth are further hidden by the skewed plot scales. The X and Y scales are in hundreds of kilometers, whereas the Z scale is in tens of meters. In the deeper areas of the domain, the evolving zero level set is abruptly halted and it forms a jagged surface parallel to the bottom. This is because in these regions the zero level set is close to the sea floor. We prohibit the zero level set from penetrating the sea floor (as the vehicle cannot move inside land). This is done by setting the advective velocity field $\mathbf{V}$ as well as the vehicle speed F_v to zero at these depths, which ensures that the optimal path never crosses through any land mass.

We observe that the initial reachable set for the AUV is quickly advected northwards due to the local northward flow at the start point, and hence fails to see the strong Gulf Stream currents. Over August 29 and 30, the reachability front grows due to the favorable flow on the east side of the cyclonic eddy that develops to the north of the Gulf Stream (especially beyond 40 m), but is held back on the west side of this eddy. This causes a crease-like feature in the reachability front as seen in Fig. 15(c). We can also see that the northeast–southwest oriented jet north of the Gulf Stream pushes the reachability front out of the domain in the southwest corner. Finally, the reachability front reaches the destination on August 31, 2006 at 20:17:22 UTC and the corresponding optimal travel time for this vehicle is 3.84 days.

Vertical-only Propulsion Float. Fig. 16 shows the evolution of the zero level set for the float capable of slow vertical propulsion only. The growth of the zero level set still locally stops at the sea floor (or just before), ensuring that the optimal path does not go through any land mass. The evolution of the level set is comparatively slower, and it takes longer for the float to reach the destination. As the horizontal evolution of the reachability front is only due to oceanic flows, it evolves faster in the region of faster ocean currents.

We find that the reachable set of the float is initially pushed to the northwest due to the local currents just north of the Gulf Stream.

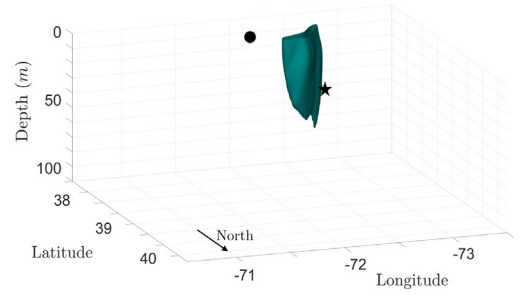

(a) Reachability front on Aug. 30, 12:00:00 UTC (2.5 days)

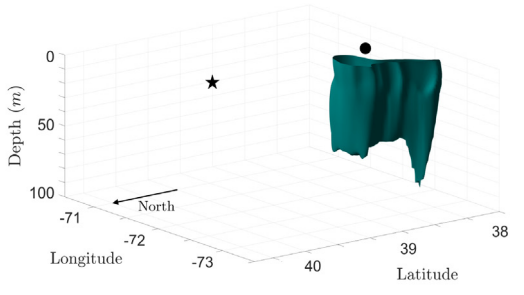

(b) Reachability front on Sept. 2, 00:00:00 UTC (5 days)

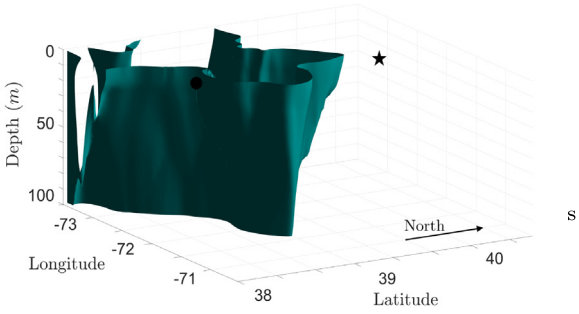

(c) Reachability front on Sept. 4, 12:00:00 UTC (7.5 days)

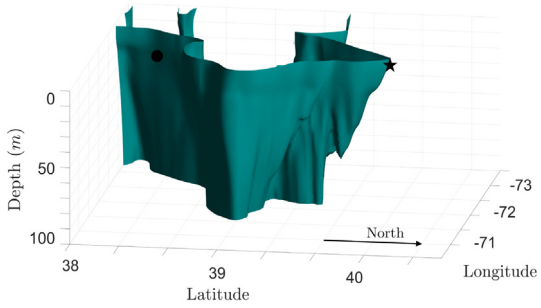

(d) Reachability front on Sept. 6, 12:40:02 UTC (9.53 days)

Fig. 16. Evolution of the zero level set (not to scale) in the Middle Atlantic Bight region for the float. This reachability front is observed to have greater variations with depth than the isotropic vehicle motion case. Further, the evolution of the level set is comparatively slower, and it takes longer for the float to reach the destination. The level set evolution is shown from different viewpoints in order to better understand the global picture.

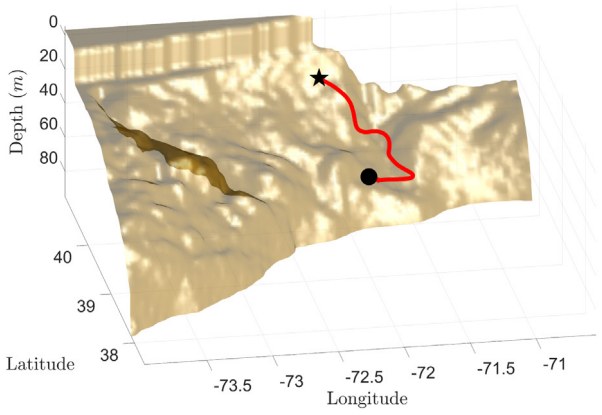

(a) Isotropic view

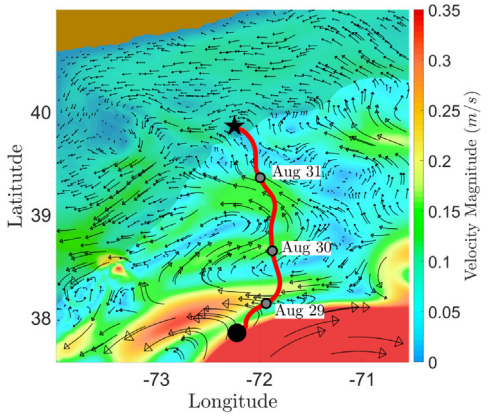

(b) Top view

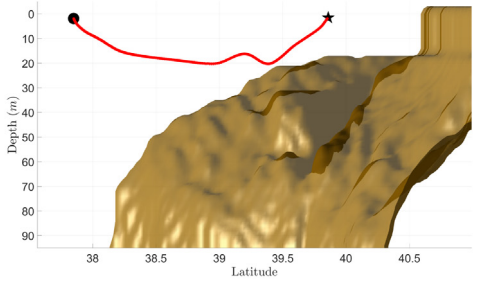

(c) Meridional view

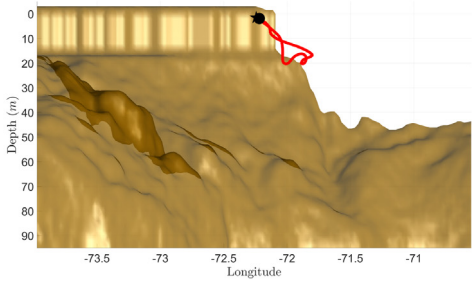

(d) Zonal view

Fig. 17. Time-optimal path predicted for an AUV with isotropic propulsion in the Middle Atlantic Bight region. Panel (a) shows the isometric view of the optimal path. Panels (b), (c), (d) depict the top, side, and front views of the path respectively. We also plot the surface velocity field on Aug. 31, 2006 at 20:17:22 UTC (*i.e.* the time at which the vehicle reaches the destination) for reference in Panel (b), along with the vehicle location at 00 UTC on August 29, 30, 31. The vehicle initially utilizes the edge of the northern wall of the Gulf Stream, and is later forced eastwards due to the flow from the Hudson Canyon. It also dives deeper in order to avoid the adverse currents at the ocean surface.

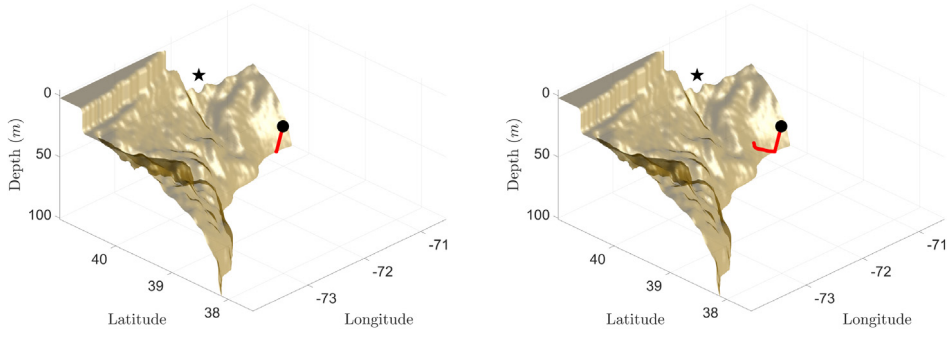

(a) Initial dive (b) Travel at constant depth

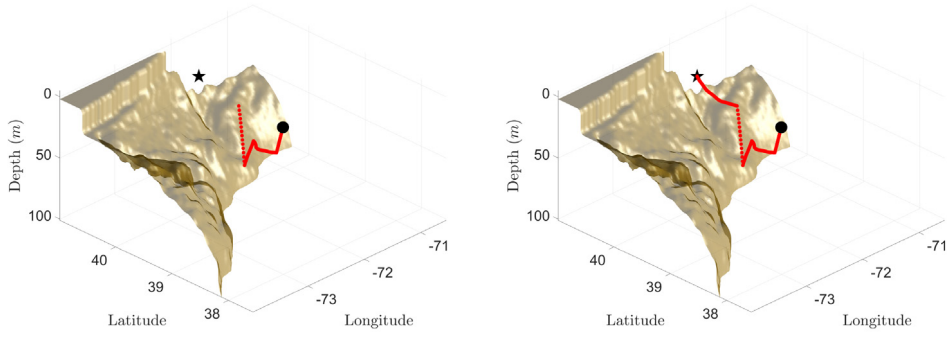

(c) Sharp dive and rise (d) Travel at the surface

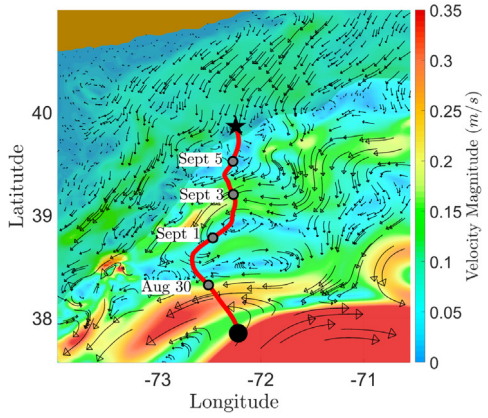

(e) Top view of the optimal path chosen

Fig. 18. Time-optimal path predicted for a float operating in the Middle Atlantic Bight region, from August 28 to September 6, 2006. We find that the float initially dives to a certain depth (about 20 m) in order to avoid the adverse flow at the surface. It then sails at this constant depth for a while. After this, it dives (down to 45 m) and rises sharply and then concludes its journey by rising the ocean surface. Dives such as the one seen in Panel (c) could be eliminated by appropriately choosing a tolerance value, see Appendix B. Finally, panel (e) shows the top view of the float path, overlaid on 20 m averaged velocity field on Sept. 6, 12:40:02 UTC (*i.e.* the time at which the float reaches the destination).

The reachability front does not reach the entire depth at all locations as the float is slower than the isotropic AUV; ocean vertical velocities may thus prohibit the float from reaching all depths of the domain. We initially observe low variation in the reachability front in the vertical, but between days 5 and 7.5 (Fig. 16(b), (c)), the reachability front grows much faster at the surface due to the favorable currents generated by tropical storm Ernesto. Ernesto's impact is limited deeper. The wind-driven response thus generates major vertical variation in the reachability front growth (much larger than that for the isotropically propelled AUV) by the time the float reaches the destination (Fig. 16(d)).

Glider. Finally, for a glider performing a sinusoidal motion in the vertical, the projected reachable set evolution is solved as a 2D problem and the projected reachability front evolved as a 2D parametric contour. If some of the points on this contour are within a tolerance of the ocean floor (or surface) at some particular time, the propulsion of the glider is then reversed only at these points. The vehicle can continue to move in the same direction at all other points until it either reaches the tolerance to the bottom or the maximum allowable depth (or surface). The location and time data of points at which such reversal of direction occurs are kept in memory and enforced while backtracking the optimal path. While planning paths for such vehicles with known vertical motion, it might happen that the vehicle reaches the horizontal coordinates of the target, but at a different depth. In such cases, one can assume that the vehicle can rise/sink locally to reach the exact target depth. This is what is done in the present example, but one could of course continue the level set computation until both the horizontal coordinates and proper depth are reached.

6.4. Three-dimensional time-optimal paths

We now examine the time-optimal paths for the three different types of vehicles considered, their characteristic features, and how they related to the ocean flows experienced by these vehicles.

6.4.1. Vehicles with isotropic speeds

Fig. 17 depicts the optimal path followed by the isotropically propelled AUV, which requires a total travel time of 3.84 days. To compare, in the absence of currents, the vehicle would travel in a straight line joining the start and target positions and would require 4.97 days. Hence, it is clear that the optimal AUV can here make efficient use of the oceanic velocities to reach the target in the shortest amount of time.

Initially, the optimal AUV is advected north by the local northward currents at the start point. It then dives deeper as the northeast-to-southwest jet to the north of the Gulf Stream is strong near the surface on August 29 (surface currents are small on August 28, but increase significantly by August 29, and hence the AUV starts to dive). It is clear in Fig. 17(b) how the AUV navigates around the southwestward currents north of the Gulf stream. By August 30 and 31, the AUV sails northward, using the favorable flow on the eastern side of the cyclonic eddy (Figs. 12(c), 13(c)) that develops to the north of the Gulf Stream (beyond 10 m depth). Around August 31, the AUV starts rising as the wind-driven currents around 10 m depth are northwestward and favorable (Fig. 12(d)) while those at the surface and 20 m are westward or southwestward and not favorable (Figs. 11(d), 13(d)). Finally, the impact of the tropical storm Ernesto causes favorable surface currents from September 1 onwards and hence the AUV rises to utilize these flows and ultimately reach the destination. Another interesting observation relates to the spacing between daily vehicle positions (Figs. 11(a)–(d), 12(a)–(d), 13(a)–(d)). It shows that the AUV travels more on the second day than on the first, and even more on the third and fourth days. This is because on the first day and a part of the second day, the AUV is traveling against southwestward currents. However, once out of this adverse currents region, it utilizes the favorable currents (eastern edge of the cyclonic eddy and those driven by Ernesto) on days 3 and 4, and thus travels larger distances.

The computational time required for the forward evolution of the reachability front for the isotropic AUV is 109.2 min for the numerical schemes of Section 4, whereas the time required for backward tracing of the optimal path is 38 s. As expected, the computational time required for backward tracing is much less than that required for the forward evolution, as one only solves an ODE in backtracking the optimal path, whereas a PDE is solved on the entire 3D domain for the forward evolution. Importantly, since the optimal travel time is 3.84 days, such exact-PDE path planning can be completed in real-time.

6.4.2. Vehicles with anisotropic speeds

For vehicles with constrained motion, we resort to an offline maximization table to compute the optimal propulsion term, as described in Appendix B. Fig. 18 shows the optimal path to be followed by the float (propulsion only in the vertical direction). The float is much slower than the isotropic propelled AUV, with a total travel time of 9.53 days. This is expected, as the float does not have any horizontal propulsion of its own. Further, we can tune a tolerance parameter of the vehicle (ref. Appendix B) such that unless a major event happens, the float tends to stay at the same depth.

The float initially dives to avoid adverse southwestward currents at shallow depths, north of the Gulf Stream (see Fig. 11), and utilizes west-northwestward currents around the start point at 20 m depth. On August 29 and 30, it advects east-northeastward with a favorable current that is present at 20 m depth, just to the north of the Gulf Stream (see Fig. 13(b), (c)). However, this current changes direction around Sept. 1 due to tropical storm Ernesto, and the float thus dives deeper, down to about 45 m, to avoid the effect of this adverse change.

On September 2 and 3, tropical storm Ernesto induces favorable velocities at the surface. Thus, the float quickly rises to the surface to capture these currents (deeper velocities on these days are unfavorable). Note that, such frequent dives can be eliminated to respect the limits on the functional characteristics of the specific float by setting the appropriate value of a tolerance parameter of the float (ref. Appendix B). Finally, post Ernesto, the current magnitudes and variations are typically small, and hence the float does not perform any vertical motion and is simply advected to reach the target.

The computational time required for the forward evolution of the reachable set and backtracking the optimal path for the float is 188.6 min and 32 s respectively. The forward evolution takes longer than that of the isotropic AUV because even though the cost per time step is comparable, the float simply takes longer to reach the destination (9.53 days), leading to higher a computational expense.

6.4.3. Vehicles with partially known motion

For vehicles with partially known motion, we solve for the 2D projection of the forward 3D reachable front. To backtrack the full 3D optimal path, we thus add back the deterministic displacement due to the vertical motion of the vehicle to the optimal projected path being backtracked in 2D. Fig. 19 shows that 3D optimal path, as predicted for a glider performing a sinusoidal yo-yo motion. The time for this journey is 4.15 days (almost 25 dives), which is slower than for the AUV with isotropic speed, but much faster than for the float. This is expected, as we impose no constraints on the motion of the AUV in the first case, whereas stricter constraints are enforced on the float motion. Note that for the last dive, the glider is also close to the sea floor and hence it terminates the dive earlier in order to not collide with the bottom.

The optimal path qualitatively follows a pattern similar to isotropically propelled AUV, but with larger deviations from horizontally straight lines. From Fig. 19(b), we find that the glider initially utilizes the northern edge of the Gulf Stream to move eastwards and so avoid the large patch of southwestward currents just to the northwest. From August 31 to September 1, it then advects north, to hop on the moderately strong north to northwestward flow (part of the eddy). Finally, when just to the south of the target, it leaves this flow (which is now westward) early on September 2, and travels north to reach the target. Similar to the isotropically propelled AUV, we can draw interesting remarks by looking at the spacing between the daily glider positions (Fig. 14(a)–(d)). The glider covers a large distance on the first day but travels a smaller one on the second. This is because it utilizes the favorable Gulf Stream to initially travel east, but then has to cross the southwestward jet only using its own speed. It later travels large distances again on the third day, this time by utilizing the north to northwestward eddy. Finally, it covers a moderate distance on the fourth day (*i.e.* more than day 2 but less than days 1 and 4) to finally reach the destination.

For the glider with a sinusoidal motion in the vertical, it takes 4.9 min to solve the level set PDE to compute the forward evolution of the reachability front, and 52 s to compute the time-optimal path by backward tracing. When compared to the corresponding computational times for the isotropic AUV (109.2 min for forward evolution, 38 s for backward tracing), we can clearly see that the forward evolution for the glider is much faster, because the level set PDE is now only solved in 2D instead of 3D. However, the backward tracing for the glider takes slightly longer as one needs to compute the contribution in the horizontal and the vertical, and then combine them to yield the optimal travel direction. Of course, the marginal cost increase in solving the backtracking ODE is overshadowed by the significant gain in the solving the forward evolution PDE.

Fig. 20 shows a top view of the optimal trajectories for the isotropic AUV, float, and glider. We find that the glider, with its forced yo-yo motion in the vertical between 0 and 90 m, makes the most use of the Gulf Stream. The AUV and float (no such forced motion) remain mostly at shallower depths and utilize favorable dynamic eddies, meanders,

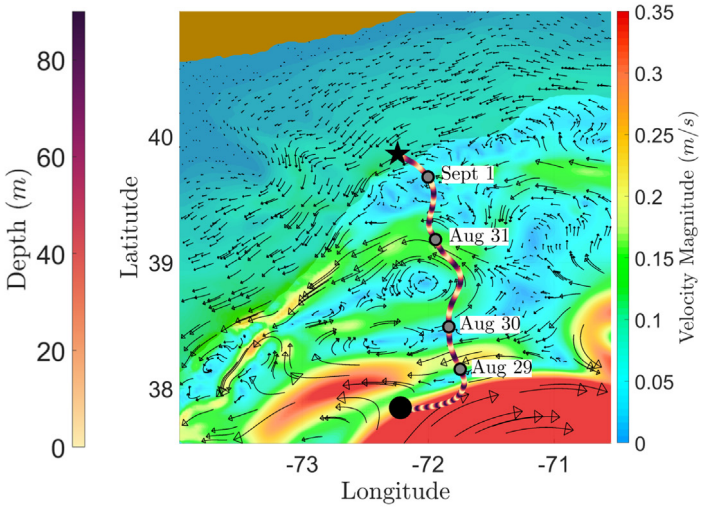

(a) Top view (path colored according to the instantaneous depth of travel)

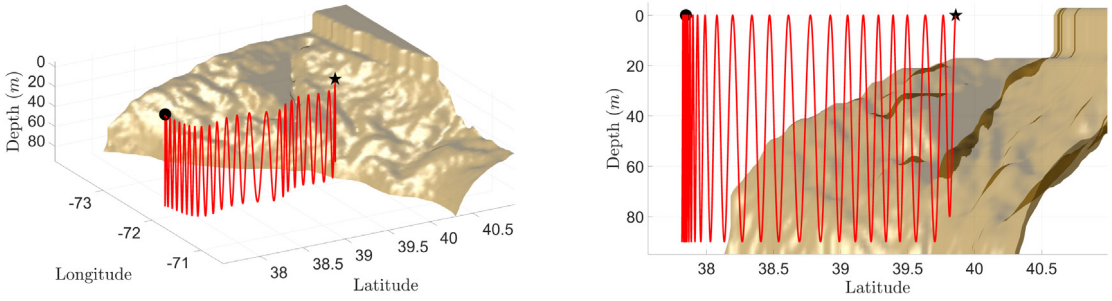

(b) Isometric view **(c)** Side view

Fig. 19. Time-optimal path predicted for a glider from August 30 to September 2, 2006 in the Middle Atlantic Bight region. We also plot the top 90 m averaged velocity field on Sept. 1, 3:35:52 UTC (*i.e.* the time at which the glider reaches the destination) for reference in Panel (a). The glider performs a yo-yo motion with dives up to 90 meters deep, and completes approximately 25 dives while traveling to the destination, requiring 4.15 days for the journey. For the last dive, the glider does not dive to 90 m due to the obstruction from sea floor.

and sub-surface currents to the north of the Gulf Stream to optimally reach the destination. The float avoids the Gulf Stream, in part to avoid challenges escaping it which would prevent reaching the target in fastest time, if at all (since the float can only move up and down).

7. Conclusions

In this paper, we first developed the theoretical foundations and practical aspects of exact time-optimal path planning in 3D realistic ocean fields with strong and dynamic currents. Specifically, we provided new extensions for the exact and efficient computation of optimal paths for commonly employed marine vehicles, respecting their motion constraints. We considered three main classes of propulsion behaviors: unconstrained isotropic, anisotropic, and partially imposed. For the latter two motions, we specialized the exact reachability PDE (Lolla et al., 2012; Lolla, 2016; Lolla and Lermusiaux, 2020) to vehicles that can propel only in certain directions (e.g. only vertical propulsion) or that have partially known motions (e.g. forced yo-yo motions), respectively. We showed that the 3D problem can be reduced to two dimensions if the motion of the vehicle is partially known, such as gliders performing deterministic oscillatory vertical motions or propelled AUVs forced to use specific patterns in the horizontal. As a result, the computational cost is reduced significantly.

Second, we obtained robust numerical schemes to solve the path planning equations consistently and with high accuracy in realistic 3D ocean domains. Since these domains have length and velocity scales that are much smaller in the vertical than the horizontal, even small numerical errors along a certain dimension may have drastic consequences along the other dimensions. To overcome this ill-scaling, we obtained the non-dimensional form of the Hamilton–Jacobi

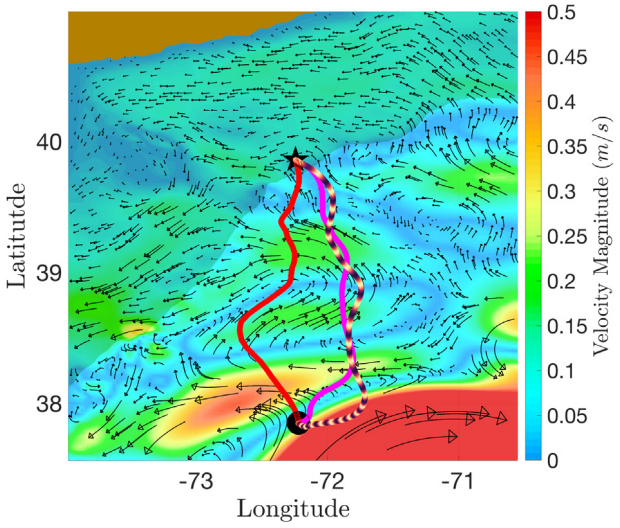

Fig. 20. Time-optimal paths predicted for the isotropic AUV (pink), float (red), and glider (colored according to depth, ref. Fig. 19) in the Middle Atlantic Bight region. We find that the prescribed deeper-diving glider uses the Gulf Stream more to its advantage than the isotropic AUV and the float that instead use shallower eddies and favorable circulation patterns to the north of the Gulf Stream.

level set equation. We next emphasized the new concept of numerical consistency between the discrete forward evolution of the reachable set and discrete backward tracing of the optimal path. We discussed high-order spatial and temporal numerical schemes for the forward evolution of the zero level set function and developed novel consistent implicit schemes for the backward tracing of the optimal path.

Third, we applied our schemes to analytical and realistic flows, integrating ocean modeling with 3D path planning with motion constraints. We validated the theory, verified schemes, and benchmarked accuracy using three analytical 3D flows. Numerical discretization errors were quantified by comparison to the analytically optimal paths and durations. The capability of correctly handling dynamic 3D flows was confirmed. Using the data-assimilative ocean currents of the MSEAS primitive-equation modeling system in the Middle Atlantic Bight region, reachability fronts and optimal trajectories were predicted and analyzed for three classes of marine vehicles, namely propelled AUVs, floats, and gliders. We described the regional ocean dynamics and the evolution of the reachability fronts in response to the instantaneous dynamic currents and propulsion characteristic of each vehicle type. We found that the effects of 3D multiscale ocean currents on the actual optimal paths chosen by the vehicles were significant, and that the vehicles tried to best utilize the favorable flow features, while avoiding the adverse flows. For such paths, ocean forecasts should be employed for real-time planning of efficient autonomous missions, from optimal pick-up and deployment, to monitoring and adaptive data collection.

In the future, since the 3D path planning PDE and ODE are exact, they can be employed in any regions and dynamics, e.g. low-order flows such as in the Sargasso sea, vertically complex flows such as in Equatorial regions, strong and complex 3D flows such as in estuaries, or in regions with physical obstacles (Lolla et al., 2015; Subramani et al., 2017b). Numerically, to further reduce the computational cost of the reachable set evolution, the narrow band level set method (Adalsteinsson and Sethian, 1995; Lolla, 2016; Lolla and Lermusiaux, 2020) could be utilized in 3D. In that case, only the values of the level set function that are strictly needed in the vicinity of the zero level set are computed. Another possible future direction is to study energy optimal paths or optimal paths in stochastic environments for such marine vehicles (Subramani et al., 2017a, 2018; Subramani and Lermusiaux, 2019). Finally, onboard routing can be implemented using the developed theory and framework (Lermusiaux et al., 2016). Vehicle positions could be assimilated to correct the predicted advective velocity field, and a modified optimal trajectory could be computed online from the real-time position of the vehicle.

CRediT authorship contribution statement

Chinmay S. Kulkarni: Conceptualization, Methodology, Software. **Pierre F.J. Lermusiaux:** Conceptualization, Methodology.

Declaration of competing interest

The authors declare that they have no known competing financial interests or personal relationships that could have appeared to influence the work reported in this paper.

Acknowledgments

We thank the members of our MSEAS group for insightful discussions. We also thank the four anonymous reviewers for their useful comments. We are grateful to the Office of Naval Research, United States of America for support under Grants N00014-14-1-0476 (Science of Autonomy LEARNS) and N00014-15-1-2616 (DRI-NASCar) to the Massachusetts Institute of Technology (MIT), United States of America. The MSEAS SW06-AWACS-06 ocean re-analyses employed were made possible by research support to MIT from ONR, United States of America under grants N00014-11-1-0701 (MURI-IODA) and the National Science Foundation, United States of America under grant OCE-1061160. We thank all of our SW06 and AWACS-06 colleagues, especially G. Gawarkiewicz, P. Abbot, and T. Duda for their ocean data and M. Taylor and J. Hare for their NMFS survey data. We also thank J. Evans, S. Glenn, and J. Wilkin for their real-time WRF atmospheric fluxes and the FNMOC teams for their products.

Appendix A. Theoretical results on the reachability set evolution

In what follows, we state the evolution of the reachability front governed by a Hamilton–Jacobi equation. Specifically, the following theorem provides the evolution of the reachable set by means of a PDE and the optimal vehicle heading function that minimizes the total travel time. The result is related to the principle of minimum action (here time) of classical mechanics.

Theorem. *Let $\mathbf{V}(\mathbf{x},t)$ be a Lipschitz continuous and bounded velocity field in all its arguments. Denote the set of permissible unit heading directions by $\mathcal{H}$, which is a subset of $\mathbb{R}^3$. Let the maximum vehicle speed $F(\hat{\mathbf{h}},t) : \mathcal{H}\times[0,\infty) \to \mathbb{R}^+$ be Lipschitz continuous in all of its arguments. We assume that the possible vehicle trajectories $\mathbf{X}(t)$ are governed by Eq. (1), with initial condition $\mathbf{X}(0) = \mathbf{x}_s$. Then, the evolution of the reachability front is given by the zero level set of the function $\boldsymbol{\phi} : \mathbb{R}^3 \times [0,\infty) \to \mathbb{R}$, where $\boldsymbol{\phi}(\mathbf{x},t)$ is the unique viscosity solution of the following equation,*

$$\frac{\partial \boldsymbol{\phi}}{\partial t} + \max_{\hat{\mathbf{h}}} \left(F(\hat{\mathbf{h}},t)\hat{\mathbf{h}}(t)\cdot\nabla\boldsymbol{\phi}\right) + \mathbf{V}(\mathbf{x},t)\cdot\nabla\boldsymbol{\phi} = 0\,, \tag{A.1}$$

with the initial conditions,

$$\boldsymbol{\phi}(\mathbf{x},0) = |\mathbf{x}-\mathbf{x}_s|\,. \tag{A.2}$$

The optimal arrival time $\mathbf{T}(\mathbf{x}_f : \mathbf{x}_s, 0)$ satisfies

$$\mathbf{T}(\mathbf{x}_f : \mathbf{x}_s, 0) = \inf_{t\geq 0}\left\{ t \mid \boldsymbol{\phi}(\mathbf{x}_f,t) = 0\right\}\,. \tag{A.3}$$

The optimal trajectory (or trajectories) $\mathbf{X}(t)$ is given by the characteristic lines of Eq. (A.1). That is, $\mathbf{X}(t)$ satisfies the following equation,

$$\frac{d\mathbf{X}}{dt} = F(\hat{\mathbf{h}},t)\hat{\mathbf{h}}(t) + \mathbf{V}(\mathbf{X},t)\,, \tag{A.4}$$

where

$$\hat{\mathbf{h}}(t) = \arg\max_{\hat{\mathbf{h}}} \left(F(\hat{\mathbf{h}},t)\hat{\mathbf{h}}(t)\cdot\nabla\boldsymbol{\phi}\right)\,. \quad \square \tag{A.5}$$

We refer to Lolla and Lermusiaux (2020) and Lolla (2016) for the proof of this theorem.

Remarks.

- It is assumed that the external velocity field $\mathbf{V}(\mathbf{x},t)$ is deterministic. In real ocean applications, the forecast fields are always associated with some uncertainty (Lermusiaux, 2006; Lermusiaux et al., 2006). However, the present results can be utilized to predict a sample path for a specific velocity realization or the path corresponding to the mean or the mode of the velocity field in such cases. Recent results by Wei (2015), Subramani et al. (2018) and Subramani and Lermusiaux (2019) are indeed build upon such ideas to predict and study time-optimal paths in stochastic flow environments.
- In this work, we only seek time-optimality. In many cases, optimality in some other objective function, such as energy spent, quality of data collected, etc., may be desired. The present results can be extended to optimize a general objective function that depends on the travel time, followed trajectory, and possible other parameters. We refer the reader to Subramani and Lermusiaux (2016) for energy optimization and to Lolla (2016) for computing optimal sampling locations. In Subramani et al. (2018) and Subramani (2018) risk-optimal trajectory is studied, depending on the whether the user is risk seeking, risk neutral, or risk averse.

- For the case where the vehicle has a heading-independent (isotropic) speed, we have $F = F(\hat{\mathbf{h}}, \mathbf{X}, t)$. This simplifies Eq. (A.1) to yield Eq. (A.6).

$$\frac{\partial \boldsymbol{\phi}}{\partial t} + F|\nabla \boldsymbol{\phi}| + \mathbf{V}(\mathbf{x}, t) \cdot \nabla \boldsymbol{\phi} = 0 \,. \tag{A.6}$$

Further, the optimal headings in this case are given by Eq. (A.7), which are just the local outward normals to the reachability front,

$$\hat{\mathbf{h}}(t) = \frac{\nabla \boldsymbol{\phi}}{|\nabla \boldsymbol{\phi}|} \,. \tag{A.7}$$

Appendix B. Numerical schemes for the forward reachable set evolution

Advection term. The numerical schemes discretizing the advection term utilize the given velocity field explicitly, and find suitable approximations for $\nabla \boldsymbol{\phi}$ by using the sign of this known velocity field. Essentially non-oscillatory (ENO) schemes and their extension to weighted essentially non-oscillatory (WENO) schemes for Hamilton–Jacobi equations (Shu and Osher, 1988; Jiang and Shu, 1996) with up to 5th order accuracy are used to in the present work. The general unsteady Hamilton–Jacobi equation only contains at most the first derivatives of the unknown function $\boldsymbol{\phi}$ (Crandall and Lions, 1983; Osher and Fedkiw, 2006) and ENO and WENO schemes provide accurate estimates.

Handling of anisotropic speeds. If the propulsion speed of the vehicle depends on the direction of travel, the optimal propulsion term is given by:

$$\max_{\hat{\mathbf{h}}(\mathbf{x},t)} \left(F(\hat{\mathbf{h}}, t)\hat{\mathbf{h}}(\mathbf{x}, t) \cdot \nabla \boldsymbol{\phi} \right) \tag{B.1}$$

This in general cannot be reduced further. In order to compute the contribution of this term, a maximization is required to be performed at each point in the domain, at all times. We discuss some approaches to solve this maximization problem.

The most general way to solve the maximization is to construct a look-up table prior to the forward evolution (Lolla, 2016; Lolla and Lermusiaux, 2020). This table holds the optimal heading directions for all possible reachability front gradient directions. That is, given the local outward normal $(\nabla \boldsymbol{\phi}(\mathbf{x}, t)/|\nabla \boldsymbol{\phi}(\mathbf{x}, t)|)$, the table returns the maximum value of the optimal propulsion term and the corresponding $\hat{\mathbf{h}}(\mathbf{x}, t)$ (required for backward tracing of the optimal path). If the vehicle is permitted to only travel along certain directions then the maximum is calculated over all the directional derivatives along the permitted directions. Care needs to be taken in making sure that the discretization for computing the optimal heading is consistent with the grid discretization, otherwise unfavorable errors may be introduced.

Such a maximization can also be performed after every time step while the forward evolution of $\boldsymbol{\phi}$ is being carried out. This is called 'online maximization'. In this case, the optimal heading direction is computed at each point and at each time by testing all permissible heading directions and choosing the maximum.

Often, offline maximization is computationally favorable (especially when the speed does not vary with time) as the propulsion term is only required to be computed once per heading direction. If the maximum speed varies with time, then the online maximization may prove to be more efficient, as in such a case the offline table has to be separately constructed for each time.

Tolerance Parameter for Discrete Anisotropic Speeds. For vehicles with propulsion speeds that are only in specific discrete directions (e.g. only up or down), a tolerance parameter to limit the frequency of direction switch can be needed. This is to avoid an optimal path with too many oscillations. This occurs if the optimal propulsion term is close to zero or if it frequently flips signs. These oscillations may not always be sufficiently accurate (sub-grid-scale process or numerical diffusion effects) and an actual marine vehicle typically should avoid such quick movements. If such oscillations occur, a simple approach to eliminate them is to use a tolerance parameter. That is, we then only consider the contribution due to the optimal propulsion term if its magnitude is larger than some tolerance value τ. The value of τ controls the amount of switches in discrete propulsion direction in the optimal path. Of course, setting this value to be too high can cause the path to deviate from optimality.

Time marching. All the temporal schemes used are total variation diminishing Runge–Kutta (TVD RK) with up to 3rd order accuracy (Gottlieb and Shu, 1998; Osher and Fedkiw, 2006). TVD RK schemes guarantee that no spurious oscillations are produced due to the temporal discretization as long as no spurious oscillations in time are produced with the forward Euler scheme, which is the building block of these schemes. The first order accurate TVD RK scheme is just the standard forward Euler time marching scheme, whereas the second order TVD RK scheme is Heun's method. The reader is referred to Osher and Fedkiw (2006) for the details of the third order accurate TVD RK time marching.

Appendix C. Numerical schemes for the backward tracing of the optimal path

The optimal path is obtained by solving the ODE given by Eq. (C.1) backward in time,

$$\frac{d\mathbf{X}}{dt} = \mathbf{V}(\mathbf{X}, t) + F\hat{\mathbf{h}}(\mathbf{X}, t) \,, \tag{C.1}$$

with the initial condition $\mathbf{X}(t = \mathbf{T}(\mathbf{x}_f : \mathbf{x}_s, 0)) = \mathbf{x}_f$. For the case of vehicles with isotropic speeds, the optimal heading $\hat{\mathbf{h}}(\mathbf{X}, t)$ is given by the local normal to the reachability front at the location $\mathbf{X}$ at time t. For vehicles with anisotropic speeds, the maximization table is used wherein the local normal direction is given as an input to obtain the optimal hading direction. Hence, in either cases, efficient computation of the normal direction to the reachability front in three dimensions is required.

Computation of normals. The reachability front is represented by multiple triangular surfaces (for curved surfaces, see Ueckermann and Lermusiaux (2010)). The vertices of all these triangles along with the corresponding connectivity matrix are stored. The procedure to compute the normal direction to a general surface is as follows:

1. The triangle to which the given point belongs is found out.
2. The normal direction to the plane of this triangle is computed by calculating the cross product of the edge vectors. This normal is placed at the centroid of the triangle.
3. Normal directions at the vertices of this triangle are computed. For each of the vertex points, the normals to all the triangles that have the said point as a vertex are first computed. As shown in Fig. C.21, the normal direction at this vertex is then given by a weighted combination of the constituent triangle normal directions, where the weights are proportional to the angle subtended by the corresponding triangle at the concerned vertex.
4. Once the normals at each of the vertices and the centroids are computed, the normal at the given point is computed by a weighted average of these 4 normals, where the weights are proportional to the distance between the given point and the location of the normal.

Backtracking schemes. We now derive various backtracking schemes that are numerically consistent with the corresponding forward evolution schemes. We only discuss the schemes for vehicles with isotropic speeds. The extension to vehicles with anisotropic speeds is straightforward through the use of the maximization table as mentioned before. Since the forward evolution is explicit, all these backtracking schemes of optimal paths are implicit, and iterative solves are required at each time step. Our naming convention is such that the references to the

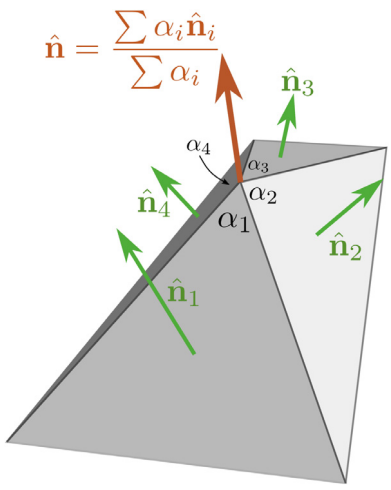

Fig. C.21. Computation of normals at the vertices and at the required point. To compute the normal direction at the vertex ($\hat{\mathbf{n}}$), we consider the weighted average of the normals of all the triangles that have the considered point as a vertex ($\hat{\mathbf{n}}_i$), where the weighting factor is the angle subtended by each of the triangles at this vertex (α_i). Once the normals at all the vertices are computed, these normals along with the surface normal (situated at the centroid) are used to compute normal at the required point (not shown).

backtracking schemes are made by the corresponding forward evolution schemes. For example, the backtracking scheme corresponding to the forward Euler temporal evolution of the PDE is referred to as the forward Euler backtracking scheme. Hence, even though the name of the backtracking scheme suggests explicit nature, they indeed are implicit.

We use the superscript $\langle \bullet \rangle$ to represent the iteration number at a specific temporal instant. The time is indicated in index form (indexed with an interval of Δt) and denoted as a subscript. The stopping criterion used for all the schemes is given by Eq. (C.2), where ϵ is a small number, typically of the order of the smallest cell size,

$$\text{Stop if} \quad |\mathbf{X}^{\langle k+1 \rangle} - \mathbf{X}^{\langle k \rangle}| \leq \epsilon \ . \tag{C.2}$$

Forward Euler backtracking. This first backward tracing scheme mimics the forward Euler scheme for the evolution of the level set function, and serves as a building block for the higher-order schemes:

$$\mathbf{X}_p^{\langle k+1 \rangle} = \mathbf{X}_{p+1} - \Delta t \cdot \left(F\hat{\mathbf{h}}(\mathbf{X}_p^{\langle k \rangle}, p\Delta t) + V(\mathbf{X}_p^{\langle k \rangle}, p\Delta t) \right) \ . \tag{C.3}$$

As we are solving Eq. (C.3) backwards in time, the value of $\mathbf{X}_{p+1}$ is known a priori and the normal $\hat{\mathbf{h}}(\mathbf{X}_p^{\langle k \rangle}, t)$ is computed by the method described above. Note that $\mathbf{X}_p^{\langle k \rangle}$ may not in general lie on the zero level set of $\boldsymbol{\phi}(\mathbf{x}, p\Delta t)$. In such cases, the normal is computed by taking the projection of this point onto the closest constituent triangle of the zero level set surface. For convenience in the forthcoming parts, we define an operator $\mathcal{B}$ as:

$$\mathcal{B}(\mathbf{X}_p^{\langle k \rangle}, p\Delta t) = \left(F\hat{\mathbf{h}}(\mathbf{X}_p^{\langle k \rangle}, p\Delta t) + V(\mathbf{X}_p^{\langle k \rangle}, p\Delta t) \right) \ . \tag{C.4}$$

TVD RK2 backtracking. Eq. (C.5) describes the implicit backtracking scheme mimicking the TVD RK2 scheme for forward evolution,

$$\mathbf{X}_p^{\langle k+1 \rangle} = \mathbf{X}_{p+1} - \Delta t \cdot \mathcal{B}\left(\mathbf{X}_p^{\langle k \rangle} + \frac{1}{2}\Delta t \cdot \mathcal{B}\left(\mathbf{X}_p^{\langle k \rangle}, p\Delta t \right), \left(p + \frac{1}{2} \right) \Delta t \right) \ . \tag{C.5}$$

This scheme may be initiated similarly to the forward Euler backtracking scheme, with $\mathbf{X}_p^{\langle 0 \rangle} = \mathbf{X}_{p+1}$. Note that $\mathcal{B}$ is the Euler building block, and two computations of the forward Euler building block are required per iteration, doubling the computational cost per iteration.

TVD RK3 backtracking. Finally, we obtain the backward tracing scheme corresponding the TVD RK3 forward evolution scheme. Eqs. (C.7) and (C.9) are the iterative equations of this TVD RK3 backward tracing. The optimal trajectory backtracking equation corresponding to the present step is:

$$\mathbf{X}_{p+1} = \frac{1}{3}\mathbf{X}_p + \frac{2}{3}\mathbf{X}_{p+\frac{3}{2}} \tag{C.6}$$

$$\implies \mathbf{X}_p = 3\mathbf{X}_{p+1} - 2\mathbf{X}_{p+\frac{3}{2}} \tag{C.7}$$

Even though we obtain $\mathbf{X}_p$ without an iterative solve, we require the value of $\mathbf{X}_p$ at intermediate times, which requires an iterative solve.

From TVD RK3 (forward marching scheme), we know that,

$$\frac{\mathbf{X}_{p+\frac{3}{2}} - \mathbf{X}_{p+\frac{1}{2}}}{\Delta t} = \left(F\hat{\mathbf{h}}\left(\mathbf{X}_{p+\frac{1}{2}}, \left(p + \frac{1}{2} \right) \Delta t \right) + V\left(\mathbf{X}_{p+\frac{1}{2}}, \left(p + \frac{1}{2} \right) \Delta t \right) \right) \ . \tag{C.8}$$

Hence,

$$\mathbf{X}_{p+\frac{1}{2}}^{\langle k+1 \rangle} = \mathbf{X}_{p+\frac{3}{2}} - \Delta t \cdot \mathcal{B}\left(\mathbf{X}_{p+\frac{1}{2}}^{\langle k \rangle}, \left(p + \frac{1}{2} \right) \Delta t \right) \ . \tag{C.9}$$

In order to initialize this scheme, we set $\mathbf{X}_{p+\frac{1}{2}}^{\langle 0 \rangle} = \mathbf{X}_{p+\frac{3}{2}}$, similar to the earlier schemes. Eq. (C.7) is not iterative, and hence does not require any initialization.

References

Adalsteinsson, D., Sethian, J.A., 1995. A fast level set method for propagating interfaces. J. Comput. Phys. 118 (2), 269–277.

Beşiktepe, Ş..T., Lermusiaux, P.F.J., Robinson, A.R., 2003. Coupled physical and biogeochemical data-driven simulations of massachusetts bay in late summer: Real-time and post-cruise data assimilation. J. Mar. Syst. 40–41, 171–212.

Bonnin, V., 2016. From Albatross to Long Range UAV Flight by Dynamic Soaring (Ph.D. thesis). University of the West of England.

Chapman, N., Lynch, J.F., 2010. Editorial: Special issue on the 2006 shallow water experiment. IEEE J. Ocean. Eng. 35 (1), 1–2.

Connolly, C.I., Burns, J.B., Weiss, R., 1990. Path planning using Laplace's equation. In: 1990 IEEE International Conference on Robotics and Automation. IEEE, pp. 2102–2106.

Cossarini, G., Lermusiaux, P.F.J., Solidoro, C., 2009. Lagoon of venice ecosystem: Seasonal dynamics and environmental guidance with uncertainty analyses and error subspace data assimilation. J. Geophys. Res.: Oceans 114 (C6).

Coulliette, C., Wiggins, S., 2001. Intergyre transport in a wind-driven, quasigeostrophic double gyre: An application of lobe dynamics. Nonlinear Process. Geophys. 8 (1/2), 69–94.

Crandall, M.G., Lions, P.-L., 1983. Viscosity solutions of Hamilton-Jacobi equations. Trans. Amer. Math. Soc. 277 (1), 1–42.

Cushman-Roisin, B., Beckers, J.-M., 2011. Introduction to Geophysical Fluid Dynamics: Physical and Numerical Aspects, Vol. 101. Academic Press.

Edwards, J., Smith, J., Girard, A., Wickman, D., Subramani, D.N., Kulkarni, C.S., Haley Jr., P.J., Mirabito, C., Jana, S., Lermusiaux, P.F.J., 2017. Data-driven learning and modeling of AUV operational characteristics for optimal path planning. In: Oceans '17 MTS/IEEE Conference, Aberdeen.

Egbert, G.D., Erofeeva, S.Y., 2002. Efficient inverse modeling of barotropic ocean tides. J. Atmos. Ocean. Technol. 19 (2), 183–204.

Elisseeff, P., Schmidt, H., Johnson, M., Herold, D., Chapman, N., McDonald, M., 1999. Acoustic tomography of a coastal front in haro strait, british columbia. J. Acoust. Soc. Am. 106 (1), 169–184.

Fan, S., Woolsey, C.A., 2014. Dynamics of underwater gliders in currents. Ocean Eng. 84, 249–258.

Ferziger, J.H., Perić, M., Street, R.L., 2020. Computational Methods for Fluid Dynamics, Vol. 4. Springer.

Frazzoli, E., Mao, Z.-H., Oh, J.-H., Feron, E., 2001. Resolution of conflicts involving many aircraft via semidefinite programming. J. Guid. Control Dyn. 24 (1), 79–86.

Froyland, G., Padberg, K., 2009. Almost-invariant sets and invariant manifolds – connecting probabilistic and geometric descriptions of coherent structures in flows. Physica D 238 (16), 1507–1523.

Gangopadhyay, A., Robinson, A.R., Haley, P.J., Leslie, W.G., Lozano, C.J., Bisagni, J.J., Yu, Z., 2003. Feature-oriented regional modeling and simulations in the gulf of maine and georges bank. Cont. Shelf Res. 23 (3), 317–353.

Garau, B., Bonet, M., Alvarez, A., Ruiz, S., Pascual, A., 2014. Path planning for autonomous underwater vehicles in realistic oceanic current fields: Application to gliders in the western mediterranean sea. J. Marit. Res. 6 (2), 5–22.

Gottlieb, S., Shu, C.-W., 1998. Total variation diminishing Runge-Kutta schemes. Math. Comput. Amer. Math. Soc. 67 (221), 73–85.

Gould, J., Roemmich, D., Wijffels, S., Freeland, H., Ignaszewsky, M., Jianping, X., Pouliquen, S., Desaubies, Y., Send, U., Radhakrishnan, K., et al., 2004. Argo profiling floats bring new era of in situ ocean observations. Eos 85 (19), 179–184.

Haley Jr., P.J., Agarwal, A., Lermusiaux, P.F.J., 2015. Optimizing velocities and transports for complex coastal regions and archipelagos. Ocean Model. 89, 1–28.
Haley Jr., P.J., Lermusiaux, P.F.J., 2010. Multiscale two-way embedding schemes for free-surface primitive equations in the "Multidisciplinary Simulation, Estimation and Assimilation System". Ocean Dyn. 60 (6), 1497–1537.
Haley Jr., P.J., Lermusiaux, P.F.J., Robinson, A.R., Leslie, W.G., Logoutov, O., Cossarini, G., Liang, X.S., Moreno, P., Ramp, S.R., Doyle, J.D., Bellingham, J., Chavez, F., Johnston, S., 2009. Forecasting and reanalysis in the Monterey Bay/California Current region for the Autonomous Ocean Sampling Network-II experiment. Deep Sea Res. II: Top. Stud. Oceanogr. 56 (3–5), 127–148. http://dx.doi.org/10.1016/j.dsr2.2008.08.010.
Hart, P.E., Nilsson, N.J., Raphael, B., 1968. A formal basis for the heuristic determination of minimum cost paths. IEEE Trans. Syst. Sci. Cybern. 4 (2), 100–107.
Javaid, M.Y., Ovinis, M., Nagarajan, T., Hashim, F.B.M., 2014. Underwater gliders: a review. In: MATEC Web of Conferences, Vol. 13. EDP Sciences, p. 02020.
Jiang, G.-S., Shu, C.-W., 1996. Efficient implementation of weighted ENO schemes. J. Comput. Phys. 126 (1), 202–228.
Kelly, S.M., Lermusiaux, P.F.J., 2016. Internal-tide interactions with gulf stream and middle atlantic bight shelfbreak front. J. Geophys. Res.: Oceans 121, 6271–6294.
Kiraly, A.P., Helferty, J.P., Hoffman, E.A., McLennan, G., Higgins, W.E., 2004. Three-dimensional path planning for virtual bronchoscopy. IEEE Trans. Med. Imaging 23 (11), 1365–1379.
Kobayashi, T., Asakawa, K., Kawano, T., Hyakudome, T., Matsuura, M., Amaike, K.-i., Watanabe, K., Ino, T., Suga, T., et al., 2012. Deep NINJA: A new profiling float for deep ocean observation. In: The 22nd International Offshore and Polar Engineering Conference. International Society of Offshore and Polar Engineers.
Krozel, J., Lee, C., Mitchell, J.S., 2006. Turn-constrained route planning for avoiding hazardous weather. Air Traffic Control Quart. 14 (2), 159–182.
Kruger, D., Stolkin, R., Blum, A., Briganti, J., 2007. Optimal AUV path planning for extended missions in complex, fast-flowing estuarine environments. In: 2007 IEEE International Conf. on Robotics and Automation. IEEE, pp. 4265–4270.
Kulkarni, C.S., 2017. Three-Dimensional Time-Optimal Path Planning in Dynamic and Realistic Environments (Master's thesis). Massachusetts Institute of Technology, Department of Mechanical Engineering, Cambridge, Massachusetts.
Kulkarni, C.S., Lermusiaux, P.F.J., 2019. Advection without compounding errors through flow map composition. J. Comput. Phys. 398, http://dx.doi.org/10.1016/j.jcp.2019.108859.
Lanser, D., Verwer, J.G., 1999. Analysis of operator splitting for advection–diffusion–reaction problems from air pollution modelling. J. Comput. Appl. Math. 111 (1–2), 201–216.
Lentz, S.J., 2008. Observations and a model of the mean circulation over the middle atlantic bight continental shelf. J. Phys. Oceanogr. 38 (6), 1203–1221.
Leonard, N.E., Paley, D.A., Davis, R.E., Fratantoni, D.M., Lekien, F., Zhang, F., 2010. Coordinated control of an underwater glider fleet in an adaptive ocean sampling field experiment in Monterey bay. J. Field Robot. 27 (6), 718–740.
Lermusiaux, P.F.J., 1999. Data assimilation via error subspace statistical estimation, part II: Mid-atlantic bight shelfbreak front simulations, and ESSE validation. Mon. Weather Rev. 127 (7), 1408–1432.
Lermusiaux, P.F.J., 2002. On the mapping of multivariate geophysical fields: Sensitivities to size, scales, and dynamics. J. Atmos. Ocean. Technol. 19 (10), 1602–1637.
Lermusiaux, P.F.J., 2006. Uncertainty estimation and prediction for interdisciplinary ocean dynamics. J. Comput. Phys. 217 (1), 176–199. http://dx.doi.org/10.1016/j.jcp.2006.02.010.
Lermusiaux, P.F.J., Chiu, C.-S., Gawarkiewicz, G.G., Abbot, P., Robinson, A.R., Miller, R.N., Haley Jr., P.J., Leslie, W.G., Majumdar, S.J., Pang, A., Lekien, F., 2006. Quantifying uncertainties in ocean predictions. Oceanography 19 (1), 92–105.
Lermusiaux, P.F.J., Haley, P.J., Leslie, W.G., Agarwal, A., Logutov, O., Burton, L.J., 2011. Multiscale physical and biological dynamics in the philippine archipelago: Predictions and processes. Oceanography 24 (1), 70–89, Special Issue on the Philippine Straits Dynamics Experiment.
Lermusiaux, P.F.J., Haley Jr., P.J., Leslie, W.G., Logoutov, O., Robinson, A.R., 2006a. Autonomous wide aperture cluster for surveillance (AWACS): Adaptive sampling and search using predictive models with coupled data assimilation and feedback - harvard page. URL http://mseas.mit.edu/archive/AWACS/index_AWACS.html.
Lermusiaux, P.F.J., Haley Jr., P.J., Yilmaz, N.K., 2007. Environmental prediction, path planning and adaptive sampling: sensing and modeling for efficient ocean monitoring, management and pollution control. Sea Technol. 48 (9), 35–38.
Lermusiaux, P.F.J., Lolla, T., Haley Jr., P.J., Yigit, K., Ueckermann, M.P., Sondergaard, T., Leslie, W.G., 2016. Science of autonomy: Time-optimal path planning and adaptive sampling for swarms of ocean vehicles. In: Curtin, T. (Ed.), Springer Handbook of Ocean Engineering: Autonomous Ocean Vehicles, Subsystems and Control. Springer, pp. 481–498, Ch. 21.
Lermusiaux, P.F.J., Malanotte-Rizzoli, P., Stammer, D., Carton, J., Cummings, J., Moore, A.M., 2006b. Progress and prospects of U.S. data assimilation in ocean research. Oceanography 19 (1), 172–183.
Lermusiaux, P.F.J., Subramani, D.N., Lin, J., Kulkarni, C.S., Gupta, A., Dutt, A., Lolla, T., Haley Jr., P.J., Ali, W.H., Mirabito, C., Jana, S., 2017. A future for intelligent autonomous ocean observing systems. J. Mar. Res. 75 (6), 765–813, The Sea. Volume 17, The Science of Ocean Prediction, Part 2.
Lin, Y.-T., Newhall, A.E., Duda, T.F., Lermusiaux, P.F., Haley, P.J., 2010. Merging multiple-partial-depth data time series using objective empirical orthogonal function fitting. IEEE J. Ocean. Eng. 35 (4), 710–721.
Linder, C.A., Gawarkiewicz, G., 1998. A climatology of the shelfbreak front in the middle atlantic bight. J. Geophys. Res.: Oceans 103 (C9), 18405–18423.
Logutov, O.G., Lermusiaux, P.F.J., 2008. Inverse barotropic tidal estimation for regional ocean applications. Ocean Model. 25 (1–2), 17–34, URL http://www.sciencedirect.com/science/article/pii/S1463500308000851.
Lolla, S.V.T., 2016. Path Planning and Adaptive Sampling in the Coastal Ocean (Ph.D. thesis). Massachusetts Institute of Technology, Department of Mechanical Engineering, Cambridge, Massachusetts.
Lolla, T., Haley Jr., P.J., Lermusiaux, P.F.J., 2014a. Time-optimal path planning in dynamic flows using level set equations: realistic applications. Ocean Dyn. 64 (10), 1399–1417.
Lolla, T., Haley Jr., P.J., Lermusiaux, P.F.J., 2015. Path planning in multiscale ocean flows: Coordination and dynamic obstacles. Ocean Model. 94, 46–66.
Lolla, T., Lermusiaux, P.F.J., 2020. A forward reachability equation for minimum-time path planning in strong dynamic flows. SIAM J. Control Optim. Sub-judice.
Lolla, T., Lermusiaux, P.F.J., Ueckermann, M.P., Haley Jr., P.J., 2014b. Time-optimal path planning in dynamic flows using level set equations: theory and schemes. Ocean Dyn. 64 (10), 1373–1397.
Lolla, T., Ueckermann, M.P., Yiğit, K., Haley Jr., P.J., Lermusiaux, P.F.J., 2012. Path planning in time dependent flow fields using level set methods. In: IEEE International Conference on Robotics and Automation (ICRA), 14-18 May 2012. pp. 166–173.
Lozano-Pérez, T., Wesley, M.A., 1979. An algorithm for planning collision-free paths among polyhedral obstacles. Commun. ACM 22 (10), 560–570.
Lozier, M., Gawarkiewicz, G., 2001. Cross-frontal exchange in the middle atlantic bight as evidenced by surface drifters. J. Phys. Oceanogr. 31 (8), 2498–2510.
MacNamara, S., Strang, G., 2016. Operator splitting. In: Splitting Methods in Communication, Imaging, Science, and Engineering. Springer, pp. 95–114.
Mannarini, G., Subramani, D.N., Lermusiaux, P.F.J., Pinardi, N., 2020. Graph-search and differential equations for time-optimal vessel route planning in dynamic ocean waves. IEEE Trans. Intell. Transp. Syst. 21 (6), 1–13.
Mirabito, C., Subramani, D.N., Lolla, T., Haley Jr., P.J., Jain, A., Lermusiaux, P.F.J., Li, C., Yue, D.K.P., Liu, Y., Hover, F.S., Pulsone, N., Edwards, J., Railey, K.E., Shaw, G., 2017. Autonomy for Surface Ship Interception. In: Oceans '17 MTS/IEEE Conference, Aberdeen.
Mittal, S., Deb, K., 2007. Three-dimensional offline path planning for UAVs using multiobjective evolutionary algorithms. In: IEEE Congress on Evolutionary Computation, 2007. CEC 2007. IEEE, pp. 3195–3202.
Newhall, A.E., Duda, T.F., Von der Heydt, K., Irish, J.D., Kemp, J.M., Lerner, S., Liberatore, S.P., Lin, Y., Lynch, J.F., Maffei, A., Morozov, A.K., Shmelev, A., Sellers, C., Witzell, W., 2007. Acoustic and Oceanographic Observations and Configuration Information for the WHOI Moorings from the SW06 Experiment. WHOI Technical Report WHOI-2007-04, Woods Hole Oceanographic Institution.
Osher, S., Fedkiw, R., 2006. Level Set Methods and Dynamic Implicit Surfaces, Vol. 153. Springer Science & Business Media.
Pereira, A.A., Binney, J., Hollinger, G.A., Sukhatme, G.S., 2013. Risk-aware path planning for autonomous underwater vehicles using predictive ocean models. J. Field Robotics 30 (5), 741–762.
Petillot, Y., Ruiz, T., Lane, D.M., 2001. Underwater vehicle obstacle avoidance and path planning using a multi-beam forward looking sonar. IEEE J. Ocean. Eng. 26 (2), 240–251.
Pinardi, N., Lermusiaux, P.F.J., Brink, K.H., Preller, R., 2017. The sea: The science of ocean prediction. J. Mar. Res. 75 (3), 101–102, Special issue: The Science of Ocean Prediction, vol. 17 of The Sea.
Prete, J., Mitchell, J., 2004. Safe routing of multiple aircraft flows in the presence of time-varying weather data. In: AIAA Guidance, Navigation, and Control Conference and Exhibit. p. 4791.
Ramp, S.R., Davis, R.E., Leonard, N.E., Shulman, I., Chao, Y., Robinson, A., Marsden, J., Lermusiaux, P.F., Fratantoni, D.M., Paduan, J.D., et al., 2009. Preparing to predict: The second autonomous ocean sampling network (AOSN-II) experiment in the Monterey bay. Deep Sea Res. II: Top. Stud. Oceanogr. 56 (3), 68–86.
Richards, A., How, J.P., 2002. Aircraft trajectory planning with collision avoidance using mixed integer linear programming. In: Proceedings of the 2002 American Control Conference, Vol. 3. IEEE, pp. 1936–1941.
Richardson, P.L., 2012. High-speed robotic albatross: Unmanned aerial vehicle powered by dynamic soaring. URL B2Streamlines.com.
Roemmich, D., Johnson, G.C., Riser, S.C., Davis, R.E., Gilson, J., Owens, W.B., Garzoli, S.L., Schmid, C., Ignaszewski, M., 2009. The Argo Program: Observing the global ocean with profiling floats. Oceanography Society.
Rudnick, D.L., Davis, R.E., Eriksen, C.C., Fratantoni, D.M., Perry, M.J., 2004. Underwater gliders for ocean research. Mar. Technol. Soc. J. 38 (2), 73–84.
Sachs, G.P., Lenz, J., Holzapfel, F., 2013. Dynamic soaring of albatrosses over land. In: AIAA Atmospheric Flight Mechanics (AFM) Conference. p. 4842.
Schmidt, H., Bellingham, J.G., Johnson, M., Herold, D., Farmer, D.M., Pawlowicz, R., 1996. Real-time frontal mapping with AUVs in a coastal environment. In: OCEANS'96. MTS/IEEE. Prospects for the 21st Century. Conference Proceedings, Vol. 3. IEEE, pp. 1094–1098.

Sethian, J.A., 1994. Curvature flow and entropy conditions applied to grid generation. J. Comput. Phys. 115 (2), 440–454.
Shadden, S.C., Lekien, F., Marsden, J.E., 2005. Definition and properties of Lagrangian coherent structures from finite-time Lyapunov exponents in two-dimensional aperiodic flows. Physica D 212 (3), 271–304.
Shu, C.-W., Osher, S., 1988. Efficient implementation of essentially non-oscillatory shock-capturing schemes. J. Comput. Phys. 77 (2), 439–471.
Siddon, R.L., 1985. Fast calculation of the exact radiological path for a three-dimensional CT array. Med. Phys. 12 (2), 252–255.
Smith, R.N., Pereira, A., Chao, Y., Li, P.P., Caron, D.A., Jones, B.H., Sukhatme, G.S., 2010. Autonomous underwater vehicle trajectory design coupled with predictive ocean models: A case study. In: 2010 IEEE International Conference on Robotics and Automation. IEEE, pp. 4770–4777.
Stokey, R.P., Roup, A., von Alt, C., Allen, B., Forrester, N., Austin, T., Goldsborough, R., Purcell, M., Jaffre, F., Packard, G., et al., 2005. Development of the REMUS 600 autonomous underwater vehicle. In: OCEANS, 2005. Proceedings of MTS/IEEE. IEEE, pp. 1301–1304.
Strang, G., 1968. On the construction and comparison of difference schemes. SIAM J. Numer. Anal. 5 (3), 506–517.
Subramani, D.N., 2018. Probabilistic Regional Ocean Predictions: Stochastic Fields and Optimal Planning (Ph.D. thesis). Massachusetts Institute of Technology, Department of Mechanical Engineering, Cambridge, Massachusetts.
Subramani, D.N., Haley Jr., P.J., Lermusiaux, P.F.J., 2017a. Energy-optimal path planning in the coastal ocean. J. Geophys. Res.: Oceans 122, 3981–4003.
Subramani, D.N., Lermusiaux, P.F.J., 2016. Energy-optimal path planning by stochastic dynamically orthogonal level-set optimization. Ocean Model. 100, 57–77.
Subramani, D.N., Lermusiaux, P.F.J., 2019. Risk-optimal path planning in stochastic dynamic environments. Comput. Methods Appl. Mech. Engrg. 353, 391–415. http://dx.doi.org/10.1016/j.cma.2019.04.033.
Subramani, D.N., Lermusiaux, P.F.J., Haley Jr., P.J., Mirabito, C., Jana, S., Kulkarni, C.S., Girard, A., Wickman, D., Edwards, J., Smith, J., 2017b. Time-optimal path planning: Real-time sea exercises. In: Oceans '17 MTS/IEEE Conference, Aberdeen.
Subramani, D.N., Wei, Q.J., Lermusiaux, P.F.J., 2018. Stochastic time-optimal path-planning in uncertain, strong, and dynamic flows. Comput. Methods Appl. Mech. Engrg. 333, 218–237. http://dx.doi.org/10.1016/j.cma.2018.01.004.
Tang, D., Moum, J.N., Lynch, J.F., Abbot, P., Chapman, R., Dahl, P.H., Duda, T.F., Gawarkiewicz, G., Glenn, S., Goff, J.A., Graber, H., 2007. Shallow water'06: A joint acoustic propagation/nonlinear internal wave physics experiment. Oceanography 20 (4), 156–167.
Testor, P., Meyers, G., Pattiaratchi, C., Bachmayer, R., Hayes, D., Pouliquen, S., Petit de la Villeon, L., Carval, T., Ganachaud, A., Gourdeau, L., et al., 2010. Gliders as a component of future observing systems. In: OceanObs' 09.
Townsend, A., Wilber, H., Wright, G.B., 2016. Computing with functions in spherical and polar geometries I. The sphere. SIAM J. Sci. Comput. 38 (4), C403–C425.
Ueckermann, M.P., Lermusiaux, P.F.J., 2010. High order schemes for 2d unsteady biogeochemical ocean models. Ocean Dyn. 60 (6), 1415–1445. http://dx.doi.org/10.1007/s10236-010-0351-x.
Wang, Y., Chirikjian, G.S., 2000. A new potential field method for robot path planning. In: 2000 IEEE International Conference on Robotics and Automation, Vol. 2. IEEE, pp. 977–982.
Wei, Q.J., 2015. Time-Optimal Path Planning in Uncertain Flow Fields Using Stochastic Dynamically Orthogonal Level Set Equations (Bachelor's thesis). Massachusetts Institute of Technology, Department of Mechanical Engineering, Cambridge, Massachusetts.
Wheeler, M.F., Dawson, C.N., 1987. An operator-splitting method for advection-diffusion-reaction problems. In: The Mathematics of Finite Elements and Applications VI. 463–382.
WHOI, 2006. Shallow water experiment 2006 (sw06). http://acoustics.whoi.edu/sw06/.
Wilkin, J., Levin, J., Lopez, A., Hunter, E., Zavala-Garay, J., Arango, H., 2018. Coastal ocean forecast system for the US mid-atlantic bight and gulf of maine. New Front. Oper. Oceanogr. 593–624.
Williamson, D.L., Drake, J.B., Hack, J.J., Jakob, R., Swarztrauber, P.N., 1992. A standard test set for numerical approximations to the shallow water equations in spherical geometry. J. Comput. Phys. 102 (1), 211–224.
Witt, J., Dunbabin, M., 2008. Go with the flow: Optimal AUV path planning in coastal environments. In: Australian Conference on Robotics and Automation, Vol. 2008.
Wong, E., Fu, K., 1986. A hierarchical orthogonal space approach to three-dimensional path planning. IEEE J. Robot. Autom. 2 (1), 42–53.
Xu, J., Lermusiaux, P.F.J., Haley Jr., P.J., Leslie, W.G., Logutov, O.G., 2008. Spatial and temporal variations in acoustic propagation during the PLUSNet-07 Exercise in Dabob Bay. In: Proceedings of Meetings on Acoustics (POMA), Vol. 4. Acoustical Society of America 155th Meeting, p. 11.
Yan, W., Bai, X., Peng, X., Zuo, L., Dai, J., 2014. The routing problem of autonomous underwater vehicles in ocean currents. In: OCEANS 2014-TAIPEI. IEEE, pp. 1–6.
Zamuda, A., Sosa, J.D.H., 2014. Differential evolution and underwater glider path planning applied to the short-term opportunistic sampling of dynamic mesoscale ocean structures. Appl. Soft Comput. 24, 95–108.
Zhao, Y.J., 2004. Optimal patterns of glider dynamic soaring. Optim. Control Appl. Methods 25 (2), 67–89.